JM PAPERS

Spectral proper orthogonal decomposition of time-resolved three-dimensional flow measurements in the turbulent wake of the Ahmed body

C.W. Chen[1], **S. Wang**[1] **and S. Ghaemi**[1],†

[1]Department of Mechanical Engineering, University of Alberta, Edmonton, T6G 2E1, Alberta, Canada

This study investigated the turbulent wake flow behind a flat-back Ahmed body using a combination of time-resolved tomographic particle image velocimetry measurements and spectral proper orthogonal decomposition (SPOD). The experiments were conducted at a Reynolds number of $Re_H = 10\,000$, which is defined as $U_\infty H/\nu$, where U_∞ represents the free-stream velocity, H is the height of the body and ν represents the viscosity. The SPOD analysis revealed four distinct flow motions present in the wake of the Ahmed body, each occupying a specific range of Strouhal number, St_H. Here, St_H is defined as $f \times H/U_\infty$, where f is the frequency of the motion. At the lowest resolved St_H of 0.007, the system exhibited a bi-stability mode, in which the wake switched between asymmetric states consisting of a tilted toroidal vortex and a streamwise vortex. In the next St_H range of 0.014 to 0.123, the flow demonstrated swinging/flapping motions, characterized by small spanwise and vertical movements of the wake barycentre. These movements were attributed to the tilting of the toroidal vortex. The third category included the vortex-shedding motions and consisted of quasi-streamwise vortices. These vortices advected in the downstream direction, causing oblique displacements of the barycentre in the streamwise-vertical plane. The peak energy of the vortex shedding was observed at $St_H = 0.164$. Finally, shear layer instabilities induced small vertical and spanwise velocity fluctuations along the shear layers at a high St_H of 1.147.

Key words: Wakes

† Email address for correspondence: ghaemi@ualberta.ca

1. Introduction

The use of wind-tunnel testing with simplified geometries is a common method for investigating the fundamental aerodynamics of road vehicles. One widely used standard model is the Ahmed body, developed by Ahmed, Ramm & Faltin (1984), which is designed for vehicle geometries that generate large regions of separated flow. This model features a flat front face that is perpendicular to the flow, with rounded corners that connect to a long rectangular body. While the rear face of the Ahmed body can have various slant angles to mimic different types of vehicles, a flat-back Ahmed body with a rear face perpendicular to the flow has become popular for investigating bluff body aerodynamics. Other simple models with different frontal geometries and aspect ratios also produce large, separated flows with similar flow features. Examples of such models include the Windsor body (Howell, Sheppard & Blakemore 2003), the ground transportation system (Croll *et al.* 1996) and the simplified lorry model (Cabitza 2013).

The measurements of Ahmed *et al.* (1984) for a flat-back Ahmed body at a Reynolds number of $Re_H = 1.3 \times 10^6$ show that the low-pressure zone at the rear face forms approximately 72 % of the total drag force. Here, Re_H is defined as $U_\infty H/\nu$, where U_∞ is the free-stream velocity, H is the height of the rear face and ν is kinematic viscosity. In a more recent investigation at a lower Re_H of 4×10^5, Evrard *et al.* (2016) estimated that approximately 52 % of total drag is due to the low pressure at the rear face. Despite the apparent discrepancy between these two investigations, both highlight the importance of the flow motions that generate the low-pressure zone and increase the vehicle drag. Experimental and numerical investigations have identified several flow motions in the wake region, including bi-stable wake motions (Grandemange, Gohlke & Cadot 2012), vortex shedding (Khalighi, Chen & Iaccarino 2012; Grandemange, Gohlke & Cadot 2013) and bubble pumping (Duell & George 1999; Volpe, Devinant & Kourta 2015). The bi-stable and vortex-shedding motions have been confirmed by many investigations while there are still discrepancies regarding the bubble-pumping motion.

The experiments of Grandemange *et al.* (2012) demonstrated a pitchfork bifurcation in which the Ahmed body wake transitioned from a steady symmetric state into a steady asymmetric topology at $Re_H = 340$. In the asymmetric state, the recirculation zone leaned towards an arbitrary spanwise side and maintained its orientation for an indefinite time. Grandemange *et al.* (2012) showed that this asymmetry persists even in the turbulent regime at $Re_H = 9.2 \times 10^4$ although it occasionally switches from one spanwise side to another. The subsequent experiments showed that the switching in the turbulent regime is random, and the two asymmetric states are equiprobable (Grandemange *et al.* 2013; Volpe *et al.* 2015). Grandemange *et al.* (2013) also estimated that the average switching period is approximately $1000H/U_\infty$, three orders of magnitude greater than the vortex-shedding time scale. The bi-stable motion has been identified using several parameters, for example, based on the barycentre location of the wake deficit (Grandemange *et al.* 2013; Volpe *et al.* 2015; Haffner *et al.* 2020), spanwise pressure gradient on the rear face (Evrard *et al.* 2016; Li *et al.* 2016; Dalla Longa, Evstafyeva & Morgans 2019) and the leading mode obtained from the proper orthogonal decomposition (POD) of velocity field or base pressure (Volpe *et al.* 2015; Pavia, Passmore & Sardu 2018; Fan *et al.* 2020; Pavia *et al.* 2020).

The previous experimental and numerical investigations have led to a better understanding of the wake topology during asymmetric states. Using particle image velocimetry (PIV) measurements, Evrard *et al.* (2016) speculated that the mean topology of each bi-stable state consists of a large horseshoe vortex – the bound section of the horseshoe vortex crosses through the off-centred recirculation zone of the wake while

the two trailing sections extend in the downstream direction. However, Perry, Pavia & Passmore (2016*b*) proposed the presence of an additional smaller horseshoe vortex to explain a small recirculating region seen on the opposing spanwise side. Using PIV measurement in cross-flow planes, Pavia *et al.* (2018) suggested that the two horseshoe vortices are connected and form a single vortex with a relatively complex topology. Fan *et al.* (2020) also proposed a similar vortex model. In a recent investigation, Pavia *et al.* (2020) developed a reduced-order model of the wake topology by applying POD to three-dimensional (3-D) flow measurements obtained using tomographic PIV (tomo-PIV). They identified two C-shaped horseshoe vortices on each spanwise side of the wake, and showed that the vortex crossing through the larger recirculation zone was stronger. However, the vortex topologies described by Evrard *et al.* (2016), Perry *et al.* (2016*b*), and Pavia *et al.* (2018, 2020) appear different from the toroidal vortex shown by the numerical simulations of Lucas *et al.* (2017) and Dalla Longa *et al.* (2019). The instantaneous visualization of the latter investigations demonstrates a toroidal topology that is skewed to conform to the asymmetric state of the recirculation zone. The discrepancy warrants additional investigations of the wake topology during the bi-stable states.

Early evidence of periodic oscillations in the Ahmed body wake is seen in the hot-wire measurements of Duell & George (1999). The detailed measurements of Grandemange *et al.* (2013) identified two flow oscillations in spanwise and vertical directions at Strouhal numbers of $St_H = 0.127$ and 0.174. Here, St_H is defined as $f \times H/U_\infty$ where f is frequency. As expected, the vertical shedding was mainly present in the upper and lower shear layers, while the spanwise shedding was detected in the side shear layers. Volpe *et al.* (2015) and Fan *et al.* (2020) also measured similar St_H values in their experiments. Plumejeau *et al.* (2019) observed greater St_H when the Ahmed body was installed at a smaller ground clearance, but the values decreased to those reported by other investigations with increased ground clearance. The smaller time scale of the vortex-shedding motion relative to the bi-stability time scale indicates that several vertical and spanwise oscillations occur within the duration of each asymmetric state. Grandemange *et al.* (2013) discussed that the bi-stability does not affect the dynamics of vertical shedding, but it results in a one-sided spanwise shedding from the stronger vertical shear layer. This one-sided vortex shedding is consistent with large hairpin vortices shed from the skewed side of the toroidal vortex seen in the numerical investigation of Dalla Longa *et al.* (2019). However, the streamwise orientation of these hairpin vortices is opposite to the horseshoe/hairpin vortices described by Evrard *et al.* (2016), Perry *et al.* (2016*b*) and Pavia *et al.* (2018, 2020). To the authors' knowledge, it is unclear how the later vortical structures interact with the vortex-shedding mechanism.

The bubble-pumping motion was originally defined to describe streamwise expansions and contractions of the separation bubble behind axisymmetric geometries such as disks and spheres (Berger, Scholz & Schumm 1990). For axisymmetric geometries, this pumping motion occurs at low frequencies and features in-phase pressure fluctuations around the rear face of the body. For Ahmed body, Duell & George (1999) observed in-phase pressure fluctuations at St_H of 0.07 only at the two spanwise sides of the rear face. In contrast, Volpe *et al.* (2015) and Pavia *et al.* (2018) observed in-phase pressure fluctuations at the top and bottom of the rear face at a similar St_H of 0.08. These investigations attributed the in-phase pressure fluctuations to bubble-pumping motions limited to different planes of the wake. Another evidence of bubble pumping is seen in the spectra of area-averaged base pressure at $St_H = 0.04$ to 0.08 (Khalighi *et al.* 2001; Dalla Longa *et al.* 2019; Haffner *et al.* 2020). Haffner *et al.* (2020) investigated the bubble pumping using cross-sectional area and strength of separation bubble from planar PIV measurements. The spectra of these quantities showed a peak at $St_H = 0.06$, indicating energetic expansion and contraction

of the separation bubble at a low frequency. In addition, evidence of bubble pumping has also been presented based on the spatial pattern of POD modes that capture in-phase fluctuations (Volpe *et al.* 2015). The POD analysis of the velocity field by Fan *et al.* (2020) shows spatial modes that exhibit the pulsation of wake deficit and recirculation bubble in horizontal and vertical planes of the wake, respectively. Despite these observations, the detailed experimental investigation of Grandemange *et al.* (2013) did not detect any indication of bubble pumping. In summary, the presence of the bubble-pumping mode and its 3-D dynamics remain unclear.

Understanding the complete 3-D dynamics of the Ahmed body wake is a challenging task, partly due to the limitations imposed by experimental and numerical simulations. In experiments, complex 3-D motions of the turbulent flow have to be inferred from point-wise hot-wire or 2-D-PIV measurements. To address this shortcoming, Perry *et al.* (2016*a*) used tomo-PIV for 3-D wake measurements of a Windsor model. Their flow analysis was preliminary, but they highlighted the challenges regarding the number density of tracer particles and spatial-dynamic range for large-scale tomo-PIV measurements. Later, Pavia *et al.* (2020) utilized a large-scale tomo-PIV for an in-depth analysis of flow topology. Booysen, Das & Ghaemi (2022) also used 3-D particle tracking velocimetry (3-D-PTV) to investigate Ahmed body wake at various side-slip angles. Although Pavia *et al.* (2020) and Booysen *et al.* (2022) obtained 3-D measurements, hardware limitations did not allow for time-resolved analysis. As a result, their 3-D investigation was limited to ensemble averages and POD analysis, which hinders the full analysis of the flow dynamics.

The POD technique used by most previous investigations of the wake flow behind the Ahmed body and similar bluff bodies is based on the space-only formulation (e.g. POD analysis of Volpe *et al.* 2015; Perry *et al.* 2016*a*,*b*; Pavia *et al.* 2018, 2020; Fan *et al.* 2020; Podvin *et al.* 2020; Booysen *et al.* 2022). In this technique, eigenvectors and eigenvalues of the two-point 'spatial' correlation tensor result in spatial modes that are modulated in time by a set of coefficients. The space-only formulation does not require time-dependent measurements, and the coefficients of the spatial modes have random time dependence (Sirovich 1987; Schmid 2010; Towne, Schmidt & Colonius 2018). As a result, the spatial modes do not necessarily represent structures that are coherent in time and each mode may represent a mix of several flow motions with different frequencies. Such a decomposition of the velocity field is not ideal for identifying complex turbulent motions. In contrast to the space-only POD, the alternative space–time formulation decomposes the two-point 'space–time' correlation tensor into modes that each oscillate at a certain frequency (Lumley 1970; Picard & Delville 2000). This technique is referred to as spectral POD (SPOD) and requires time-dependent flow realizations. To the authors' knowledge, only Haffner *et al.* (2020) and Venning *et al.* (2022) applied SPOD to time-resolved planar PIV measurements of Ahmed body wake. The SPOD analysis of Haffner *et al.* (2020) demonstrated evidence of pumping, shedding and a localized high-frequency mode at $St_H \sim 1$, while the SPOD analysis of Venning *et al.* (2022) characterized oscillatory modes behind a slant back body when varying its aspect ratio. Although computational fluid dynamics provides time-resolved flow fields, computational resources have limited access to long data sequences suitable for SPOD. An alternative technique that can address the shortcoming of space-only POD is dynamic mode decomposition. Dynamic mode decomposition was applied by Evstafyeva, Morgans & Dalla Longa (2017) in a streamwise–spanwise plane of Ahmed body wake at $310 < Re_H < 435$, and by Dalla Longa *et al.* (2019) for a simplified lorry model at $Re_H = 20\,000$.

The present investigation employs a unique approach to investigate the turbulent motions occurring in the wake of the Ahmed body. This approach involves the utilization of time-resolved tomo-PIV to measure 3-D velocity fields. Subsequently, these velocity fields are subjected to modal decomposition using SPOD, which allows for the identification of spatial modes at specific frequencies. The results address the lingering questions regarding the 3-D topology of bi-stability, vortex shedding and shear layer instability. Additionally, the findings reveal the existence of swinging/flapping motions over a wide St_H range, which encompass certain characteristics associated with the bubble-pumping mode. In § 2, a detailed description of the experimental set-ups and the implementation of SPOD are presented. Sections 3 and 4 analyse the mean flow field and the barycentre location of the wake deficit, respectively. To facilitate comparison with existing literature, a space-only POD analysis is conducted in § 5. In § 6, the characterization of the spatio-temporal dynamics of the coherent structures using SPOD is presented. Finally, § 7 summarizes the most important observations and conclusions from this investigation.

2. Experimental methodology

The flow facility and the model's size were selected to enable time-resolved tomo-PIV within a measurement volume covering the full near-wake region. For this reason, the experiments were carried out in a water flume to benefit from two factors. First, for a desired Reynolds number, the smaller kinematic viscosity of water requires a smaller model and, therefore, a smaller measurement volume relative to experiments carried out using air in wind tunnels. Second, the density of water allows utilizing of large tracers that scatter more light for tomo-PIV imaging. Consequently, the smaller measurement volume and the larger tracer particles allowed the recording of tomo-PIV images with sufficient signal-to-noise ratio for a volumetric measurement with dimensions of $78 \times 45 \times 66$ mm^3 (equivalent to $2.6H \times 1.5H \times 2.2H$) in the streamwise ($x$), vertical ($y$) and spanwise ($z$) directions, respectively. In addition to tomo-PIV, planar PIV measurements were carried out for preliminary characterization of the flow upstream and downstream of the model. In the following sections, the flow facility, planner PIV, tomo-PIV and the implementation of the modal decomposition are described.

2.1. *Flow facility*

The test section of the water flume has a length, width and height of 5.0 m, 0.68 m and 0.50 m, respectively. Two centrifugal pumps operate in parallel to circulate the flow in the flume. The reservoir of the flume consists of guide vanes, a honeycomb structure, and two layers of mesh and is connected via a small contraction section to the downstream test section. To provide optical access, the bottom and side walls of the test section are made of glass. The free-stream speed was set to $U_\infty = 0.396$ m s^{-1} during all the measurements.

An Ahmed body was mounted upside down on a flat plate as seen in figure 1(*a*). The flat plate had a total length of 700 mm and a width of 620 mm. It featured an optimized leading-edge (LE) profile and a tapered trailing edge (Hanson, Buckley & Lavoie 2012). The Ahmed body was located along the spanwise centre of the test section, 195 mm above the bottom wall of the flume, and 126 mm below the free surface of the water flume. These distances minimized the interference of the wake flow with the boundary layer on the flume walls and the free-surface waves.

The LE of the Ahmed body was at a distance of $l_1 = 259$ mm downstream of the plate's LE. At this location, the Reynolds number, *Re*, of the boundary layer based on l_1 and U_∞, is 1.0×10^5, slightly smaller than the critical Reynolds number for natural
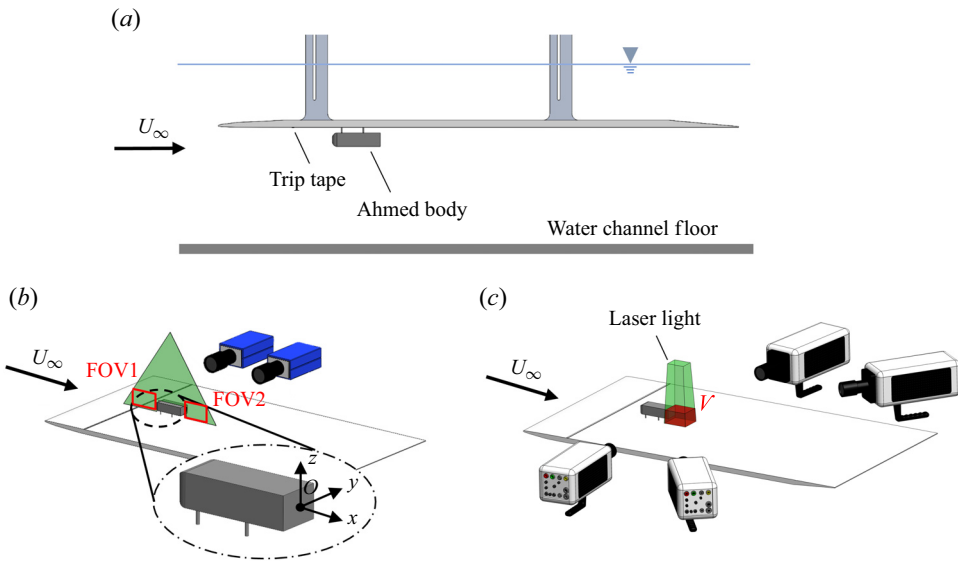
Figure 1. (*a*) Schematic of the experimental configuration showing the test section of the water flume, the flat plate and the Ahmed body. (*b*) An upside-down schematic of the flat plate, Ahmed body, the laser sheet and two cameras used for planar PIV. The coordinate system is shown in the enlarged view of the model with the origin, *O*, at the centre of the rear face. (*c*) An upside-down schematic of the tomo-PIV configuration showing the four high-speed cameras, the laser light (green) and the measurement volume *V* (red).

laminar-to-turbulent transition. Preliminary planar PIV measurements without the Ahmed body showed that the shape factor at this location was 1.86, confirming a transitional state (Schlichting & Gersten 2016). Therefore, a tripping tape with a rectangular cross-section of 1 mm × 4.5 mm (wall-normal height × streamwise length) was installed at $l_2 = 160$ mm downstream of the plate LE. The location of the tape (l_2) and height (h) were selected to ensure the laminar-to-turbulent transition according to the criteria described by Braslow & Knox (1958) and Schlichting & Gersten (2016). In addition, PIV measurements showed a shape factor of 1.47 at l_1 (without the Ahmed body), indicating that the trip wire resulted in a turbulent boundary layer. When the Ahmed body was not installed, the boundary layer thickness (based on 99 % of U_∞) at l_2 was $\delta_2 = 5.7$ mm, and at l_1 was $\delta_1 = 8.6$ mm. The distance between the tripping tape and the Ahmed body is $17.5\delta_2$, which allows sufficient flow development before the flow reaches the Ahmed body (Elsinga & Westerweel 2012).

The Ahmed body featured a flat back (no taper at the rear face) and had a 1 : 9.6 scale with respect to the original model of Ahmed *et al.* (1984). The model was machined from acrylic using a computerized numerical control router. The front and rear faces were painted in black to reduce reflections of the laser light during the experiments. The total length *L* of the model was 109.0 mm, and the height *H* and width *W* of the rear face were 30.0 mm and 40.0 mm, respectively. The uncertainty in these dimensions is approximately ±0.03 mm, accounting for potential thermal expansion or contraction of the model. The Reynolds number, defined as $Re_H = U_\infty H/\nu$, is 10 000. This Re_H matches the Re_H of recent numerical simulations by Podvin *et al.* (2020, 2021). Podvin *et al.* (2020) employed POD analysis on the flow field derived from their numerical simulation and noted a good agreement with the experimental findings reported by Evrard *et al.* (2016) at a higher $Re_H = 4.0 \times 10^5$. Consequently, based on the observations of Podvin *et al.* (2020), the flow structures characterized in the current investigation may hold relevance at higher Re_H. The model was connected to the plate using four cylinders with a

3 mm diameter. The clearance between the model and plate, C, was set to 11.2 mm. The clearance-to-height ratio of the current set-up is $C/H = 0.37$, which is larger than the $C/H = 0.17$ used by Ahmed *et al.* (1984). The larger clearance is chosen to compensate for the large $\delta_1/H = 0.29$ of the current experiment. In general, Grandemange *et al.* (2013) and Cadot, Evrard & Pastur (2015) showed that bi-stability is present when $C/H > 0.1$.

As shown from the enlarged view of the Ahmed body in figure 1(*b*), the origin of Cartesian coordinate system O is at the middle of the rear face. In the following sections, the directions of the axes are defined as x in the streamwise direction, y in the spanwise direction and z in the direction normal to the flat plate. The components of instantaneous velocity are defined as U, V and W, following the same order as the coordinate system axes. Lastly, the lowercase letters u, v and w represent the fluctuating velocity components. The mean value and the absolute magnitude of any quantity are indicated as $\langle \cdots \rangle$ and $|\cdots|$, respectively.

2.2. *Planar particle image velocimetry*

A planar PIV experiment was carried out to characterize the mean flow upstream and downstream of the Ahmed body. The PIV system consisted of two Imager ProX (LaVision GmbH) 14-bit CCD cameras with a pixel size of 7.4×7.4 µm^2. Both cameras were equipped with Nikon lenses with a focal length of $f = 105$ mm and an aperture setting of f/5.6. The upstream and downstream measurements were conducted simultaneously using a common laser sheet aligned with the x–y plane, as shown in figure 1(*b*). The first camera imaged the field-of-view (FOV) indicated as FOV1 upstream of the Ahmed body, while the second camera imaged FOV2 downstream of the model. Both cameras imaged the flow using cropped sensors with 2047×1001 pixel. FOV1 and FOV2 had similar dimensions of 146.4×71.5 mm^2 and 149.8×73.2 mm^2, respectively. The digital resolution of FOV1 was 71.5 µm pixel^{-1}, and the digital resolution of FOV2 was 73.2 µm pixel^{-1}. A dual-cavity Nd:YAG laser (Gemini, NewWave Research) with 110 mJ pulse^{-1} was used as the illumination source. Combining two cylindrical and two spherical lenses converted the laser beam into a wide sheet with 1 mm thickness covering FOV1 and FOV2. Two sets of 1500 double-frame images were collected at an acquisition rate of 9.4 Hz and with a laser pulse separation of $\Delta t = 1500$ µs.

Glass beads with the thin silver coating (SG02S40 Potters Industries) were used as tracer particles for planar PIV. These monodisperse tracers have a mean diameter of $d_p = 2$ µm and a density of $\rho_p = 4$ g cm^{-3} (Das & Ghaemi 2021). Their response time, $t_p = \rho_p d_p^2/18\mu$, and settling velocity, $u_p = (\rho_p - \rho)d_p^2 g/18\mu$, are 9.8×10^{-7} s and 7.2×10^{-6} m s^{-1}, respectively. Here, ρ and μ are water's density and dynamic viscosity, and g is the gravitational acceleration. Assuming that the flow time scale is estimated based on the vortex-shedding period ($\sim 7 \times H/U_\infty$), the Stokes number of these tracers, $Stk = t_p/t_f$, is 1.8×10^{-6}, which is smaller than the recommended value of 0.1 (Samimy & Lele 1991). The Froude number Fr is also estimated as u_p/U_∞, which is 1.8×10^{-5}, several orders of magnitude smaller than unity (Bewley, Sreenivasan & Lathrop 2008).

To improve the image's signal-to-noise ratio, the minimum intensity of all images was calculated and then subtracted from each image. The resulting images were then normalized using the average intensity of the images. The 2-D vector fields were obtained through double-frame cross-correlation with a multi-pass algorithm in Davis 8.3 (LaVision GmbH). The final interrogation window was 32×32 pixels (2.2×2.2 mm^2). A window overlap of 75 % was applied between neighbouring interrogation windows, resulting in 55 and 73 vectors along the height and width of the model, respectively.

Approximately 3 % of the velocity vectors were identified as spurious and were removed based on the universal outlier detection method (Westerweel & Scarano 2005).

2.3. *Tomographic particle image velocimetry*

The tomo-PIV system consisted of four high-speed cameras (Phantom v611, Vision Research) imaging the illuminated volume from the camera arrangement shown in figure 1(*c*). The cameras feature a complementary metal-oxide-semiconductor sensor with 1280×800 pixels; each pixel 20×20 µm^2. The two upstream cameras had a small viewing angle of approximately 5° with respect to the *z*-axis, while the two downstream cameras had a larger viewing angle of approximately 35°. To minimize image distortion at high imaging angles, the latter two cameras imaged through two water-filled prisms installed on the glass wall of the flume. The cameras had a digital resolution of approximately 70 µm pixel^{-1} and a magnification of 0.3. All cameras had Nikon lenses ($f = 105$ mm) and Scheimpflug adapters. An aperture setting of $f/22$ was used for all cameras, resulting in a depth-of-focus of approximately 66 mm.

A dual-cavity Nd:YLF laser (DM20-527DH, Photonics Industries) with 20 mJ pulse^{-1} illuminated the measurement volume. The laser light was directed perpendicular to the flat plate (in the negative *y* direction) from the bottom glass wall of the water flume. The beam passed through multiple cylindrical lenses to first form an elliptical cross-section. Then four knife edges at the bottom wall of the flume cropped the edges of the expanded beam. This resulted in a rectangular cross-section and a relatively 'top hat' intensity profile across its cross-section. The illuminated volume had a cross-section of $(\Delta x, \Delta z) = $ (85 mm, 67 mm) at $y = -H/2$ and (81 mm × 65 mm) at $y = +H/2$ plane. The measurement volume, indicated by the red colour in figure 1(*c*), had dimensions of $78 \times 45 \times \sim 66$ mm^3 ($2.6H \times 1.5H \times 2.2H$) in *x*, *y* and *z*, respectively.

To address the limited energy of the high-repetition laser, we used relatively large polystyrene spheres (TS250 Dynoseeds) with a mean diameter of $d_p = 250$ µm and density of 1.05 g cm^{-3}. The larger tracers increase the intensity of the scattered light ($\sim d_p^2$), while their nearly neutral density in water results in a small response time of $t_p = 4 \times 10^{-3}$ s. Based on the vortex-shedding time scale, the estimated *Stk* number of these particles is 7.6×10^{-3}, which is smaller than the maximum recommended value of 0.1 (Samimy & Lele 1991). The settling velocity of the tracers is also 1.9×10^{-3} m s^{-1}, and therefore their *Fr* is 4.7×10^{-3}, which is also several orders of magnitude smaller than unity (Bewley *et al.* 2008). Based on visual inspection of the tomo-PIV images, the particle image diameter is between 3 and 5 pixels, and the seeding density is 0.03 particles per pixel. Combining these two parameters results in the maximum recommended source density of $N_s = 0.3$ (Scarano 2012).

The imaging system was calibrated using a dual-plane 3-D calibration plate (type 10, Lavision GmbH) that was traversed to five *z* locations with 12 mm spacing. The mapping function of measurement volume was initially constructed using a third-order polynomial fit in Davis 8.4 (LaVision GmbH). To improve the calibration accuracy, this was followed with a volume self-calibration procedure (Wieneke 2008). Using self-calibration, the root-mean-square of the calibration error reduced from 1.3 to 0.05 pixels, which is below the recommended 0.1 pixels.

The tomo-PIV images were recorded as double-frame and time-resolved single-frame images. The double-frame images allowed for obtaining a longer duration of non-correlated data at a low acquisition frequency for faster statistical convergence. In contrast, the single-frame data at a higher acquisition frequency allowed for resolving

the high-frequency dynamics of the flow. For double-frame recording, 3 datasets of 3107 double-frame images were collected at 25 Hz using a laser pulse separation of $\Delta t =$ 3500 μs. The total duration of each set is 124.3 s, which is equivalent to $1641 \times H/U_\infty$ (larger than the bi-stability time scale of $\sim 1000 H/U_\infty$). For time-resolved measurements, 10 datasets of 6212 single-frame images were collected at a recording rate of 280 Hz. Each time-resolved dataset was 22.2 s, which is $292 \times H/U_\infty$ (shorter than the bi-stability time scale). The time-resolved data can be used for spectral analysis of the flow between St_H of 0.003 and 21.2 (half the acquisition frequency). A similar maximum particle displacement of around 18 pixels was obtained for both double-frame and single-frame images. The 10 time-resolved datasets provide the stochastic ensemble required for SPOD computations.

For processing the tomo-PIV images, first, the minimum of all images was subtracted from each image. This was followed by subtracting the local minimum of image intensity within a kernel size of 5 pixels. The images were also normalized using a local average with a kernel of 100 pixels. The measurement volume was reconstructed using the fast multiplicative algebraic reconstruction technique (fast-MART) in Davis 8.4 (LaVision GmbH) following the algorithm of Atkinson & Soria (2009). The reconstructed volume has $1116 \times 645 \times 931$ voxels in x, y, and z directions. The vector field was obtained using the direct correlation in Davis 8.4 (LaVision GmbH). The final interrogation volume was $48 \times 48 \times 48$ voxels ($3.36 \times 3.36 \times 3.36$ mm^3) with a 75 % overlap, resulting in $93 \times 54 \times 78$ vectors in the x, y and z directions, respectively. The spurious vectors formed approximately 2 % of the total number of vectors. These vectors were detected using the universal outlier detection (Westerweel & Scarano 2005) and replaced using linear interpolation. Finally, the measurement volume, V, was further cropped to $83 \times 47 \times 56$ vectors ($2.3H \times 1.3H \times 1.6H$) to remove noisy borders. The fast-MART and direct correlation processes for each single-frame dataset (6213 images) were carried out using a 16-core processor (AMD Ryzen 9 5950X) over a duration of 2 weeks.

The bi-stability motion, discussed earlier, leads to prolonged periods of spanwise asymmetry in the flow field. Consequently, achieving spanwise symmetry of time-averaged velocity fields becomes challenging, particularly for tomo-PIV measurements that generate large datasets and require intensive computations. To address this challenge, we adopt the technique utilized by Podvin *et al.* (2020) to enforce spanwise symmetry. This involves appending the original vector fields of the 10 time-resolved tomo-PIV datasets with 10 additional copies, each flipped along the spanwise direction. The copied vector fields also undergo a reversal of the spanwise velocity component to ensure a divergence-free flow field. A similar symmetrization process is also applied to the 3 double-frame tomo-PIV datasets. The resulting symmetry-enforced database eliminates any spanwise asymmetry in time-averaged fields and modal decomposition and improves the statistical convergence of the results.

2.4. *Modal decomposition*

The POD computations are carried out based on the snapshot method of Sirovich (1987) and using the 6 symmetry-enforced double-frame tomo-PIV datasets. The vector fields obtained from the double-frame images are temporally uncorrelated, resulting in faster statistical convergence of the POD modes. To begin the POD computations, three instantaneous velocity fluctuations (u, v and w) from all the grid points of each tomo-PIV snapshot were stacked into a column vector $x_i \in R^N$. Here, N equals the number of flow variables times the number of grid points ($3 \times 218\,456$). The x_i vectors were then grouped together in a 2-D matrix $\boldsymbol{X} = [x_1, x_2, \ldots, x_M] \in R^{N \times M}$ where $M = 18\,642$ is the total number of snapshots. The singular value decomposition of the correlation matrix, $\boldsymbol{X}^T \boldsymbol{X}$, was computed to obtain $\boldsymbol{U\sigma V}^T$. The parameters $\boldsymbol{U}$ and $\boldsymbol{V}$ are the left and right

matrices of eigenvectors, and $\boldsymbol{\sigma}$ is the eigenvalues matrix. The matrix of spatial modes is $\boldsymbol{\Phi} = \boldsymbol{XU\sigma}^{-1/2}$, where each spatial POD mode, Φ_j, is a column of $\boldsymbol{\Phi}$. The energy of each POD mode, σ_j, is obtained from the diagonal components of $\boldsymbol{\sigma}$. This method is equivalent to carrying out an eigendecomposition of $\boldsymbol{X}^T\boldsymbol{X}$ according to $\boldsymbol{X}^T\boldsymbol{XU} = \boldsymbol{U\sigma}^{-1/2}$ and calculating the spatial modes following $\boldsymbol{\Phi} = \boldsymbol{XU\sigma}^{-1/2}$.

An SPOD code was developed in MATLAB (MathWorks) based on the SPOD algorithm detailed by Towne *et al.* (2018). The computations used the 20 symmetry-enforced time-resolved tomo-PIV datasets, each consisting of 6212 snapshots recorded at 280 Hz. Each dataset is divided into 3 equal segments with 50 % overlap, which results in a total of $S = 60$ segments. The data within each data segment are organized in a 2-D matrix, $\boldsymbol{X}_k = [\boldsymbol{x}_1, \boldsymbol{x}_2, \ldots, \boldsymbol{x}_M] \in R^{N \times M}$, where k is the segment's index varying from 1 to 60. Similar to POD, $\boldsymbol{x}_i$ is a column-wise vector of the tomo-PIV snapshot with a length of $N = 3 \times 218\,456$. The total number of snapshots within each segment, M, equals 3106 since the segment length is half the size of the time-resolved dataset. The current segmentation procedure is slightly different from the algorithm described by Towne *et al.* (2018), in which one long dataset was divided into multiple segments. This difference is imposed by the finite onboard memory of high-speed cameras, which prevents acquiring longer datasets.

In addition, due to the limited memory of the processing computers, each data segment, $\boldsymbol{X}_k$, is processed separately. The rows of $\boldsymbol{X}_k$ matrices are multiplied by a Hamming window and then converted to the frequency domain by performing the fast Fourier transform operation. The Fourier representation of each $\boldsymbol{X}_k$ is $\boldsymbol{Q}_k = [\boldsymbol{q}_1, \boldsymbol{q}_2, \ldots, \boldsymbol{q}_K] \in C^{N \times K}$, where $\boldsymbol{q}_l$ is a column-wise vector of Fourier coefficients at frequency index l, varying from 1 to $M/2 = 1553$. The index $l = 1$ corresponds to a frequency of 0 Hz, while the last index of l corresponds to 140 Hz ($St_H = 10.6$). The resolution of the spectral domain is also 0.09 Hz (equivalent to ΔSt_H of 0.007). Next, the column vectors $\boldsymbol{q}_l$ corresponding to frequency index l from all $\boldsymbol{Q}_k$ matrices are grouped into a single matrix, $\boldsymbol{Q}'_l = [\boldsymbol{q}_l^1, \boldsymbol{q}_l^2, \ldots, \boldsymbol{q}_l^S] \in C^{N \times S}$. Once $\boldsymbol{Q}'_l$ is computed, matrix $\boldsymbol{C}_l$, for each frequency index l, is constructed as $\boldsymbol{C}_l = (1/S)\boldsymbol{Q}'^T_l\boldsymbol{Q}'_l$ using the method of snapshots (Sirovich 1987). Finally, the SPOD modes and eigenvalues are computed following $\boldsymbol{C}_l\boldsymbol{\phi}_l = \boldsymbol{\phi}_l\boldsymbol{\lambda}_l$ and $\boldsymbol{\Psi}_l = \boldsymbol{Q}_l\boldsymbol{\phi}_l$. Here, $\boldsymbol{\phi}_l$ is the eigenvector of $\boldsymbol{C}_l$, and $\boldsymbol{\Psi}_l$ includes the SPOD modes at frequency index l. The matrix $\boldsymbol{\Psi}_l$ has the form of $[\Psi_l^1, \Psi_l^2, \ldots, \Psi_l^S] \in C^{N \times S}$. The eigenvalue λ_l^n corresponding to SPOD mode n at wavenumber l is embedded in the diagonal elements of $\boldsymbol{\lambda}_l$.

In the analysis of the subsequent sections, the SPOD modes are used to reconstruct a periodic reduced-order model (ROM) at selected frequencies (Nekkanti & Schmidt 2021). The ROM model of the U component at frequency index, l, is computed according to

$$U_{ROM} = \langle U \rangle / U_\infty + \mathcal{R}e(\Psi_{u,l} / U_\infty \times e^{i\Phi}). \tag{2.1}$$

Here, $\mathcal{R}e$ is the real part of a complex number. For any grid point of the measurement domain, $\langle U \rangle$ is the average velocity, $\Psi_{u,l}$ denotes the streamwise component of SPOD mode at frequency index l. The phase Φ is also defined as $2\pi f_l t$ in which f_l is the frequency (in Hz) corresponding to index l. The duration of each ROM cycle is different as it is equal to $1/f_l$. Similar equations based on $\Psi_{v,l}$ and $\Psi_{w,l}$ are also used to reconstruct ROMs of the V and W components indicated as V_{ROM} and W_{ROM}, respectively. In addition, to reconstruct the ROM of the velocity fluctuations, (2.1) is reduced to

$$u_{ROM} = \mathcal{R}e(\Psi_{u,l} / U_\infty \times e^{i\Phi}). \tag{2.2}$$

Similar equations are also used to reconstruct v_{ROM} and w_{ROM}.
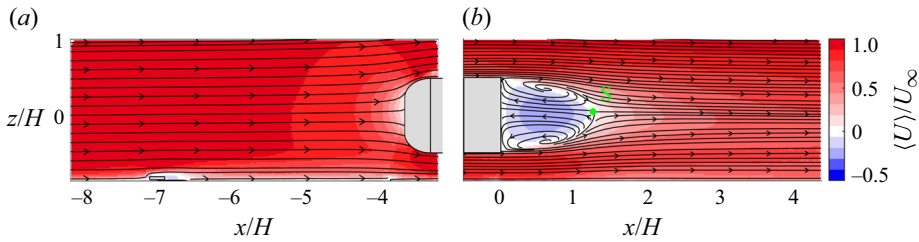
985 A19-10

Figure 2. Flow streamlines and contours of normalized streamwise velocity from planar PIV (*a*) upstream and (*b*) downstream of the Ahmed body in the $y/H = 0$ plane.

3. Mean flow characterization

This section evaluates the mean flow characteristics using planar- and tomo-PIV measurements. Figure 2(*a*) shows the $\langle U \rangle / U_\infty$ contour in the *x–z* plane upstream of the Ahmed body. A small reversed flow region is observed over the flat plate right after the tripping tape at $x/H \approx -7$. The streamlines show a parallel flow that encounters the front face of the Ahmed body, forming a stagnation point on the front face of the body at $z/H \sim 0$. In figure 2(*b*), contours of $\langle U \rangle / U_\infty$ in the *x–z* plane show a recirculation zone downstream of the Ahmed body holding two counter-rotating vortices. The strongest backflow is between the two vortices and reaches a magnitude of $\sim 0.25 U_\infty$, similar to the observations of the previous investigations (Grandemange *et al.* 2013; Volpe *et al.* 2015; Perry *et al.* 2016*a*; Fan *et al.* 2020; Pavia *et al.* 2020).

The clearance between the bottom face of the Ahmed body and the flat plate affects the underbody flow rate. If this flow rate is too small, a secondary separation bubble forms on the flat plate downstream of the Ahmed body, and the bi-stable switching of the wake disappears (Plumejeau *et al.* 2019). In figure 2(*b*), no indication of a secondary separation bubble is present, suggesting the underbody clearance is sufficient. The sufficient underbody clearance is also evident when the shear layer thickness is compared with the underbody clearance. The shear layer thickness is $0.2C$ in the current investigation, estimated based on the region of intense vorticity. This value is comparable to the shear layer thickness of $0.1C$ estimated by Grandemange *et al.* (2013) and $0.27C$ by Kang *et al.* (2021).

The length of the separation bubble, L_s, is an important parameter since it is inversely proportional to the base drag of the vehicle (Grandemange, Gohlke & Cadot 2014). This parameter can be estimated from the location of the saddle point labelled with the letter '*S*' in figure 2(*b*). The estimated L_s of the current flow is $1.24H$, which is smaller than L_s of $1.4H$ to$1.5H$ reported at higher Re_H by Grandemange *et al.* (2013), Volpe *et al.* (2015) and Fan *et al.* (2020). The smaller L_s of the current investigation is consistent with the trend observed by Plumejeau *et al.* (2019), showing that the L_s reduced from $1.41H$ to $1.31H$ when Re_H decreased from 4.29×10^5 to 1.43×10^5.

The state of the boundary layer developed on the upper surface of the Ahmed body can be evaluated by characterizing the intensity of the fluctuations. At the streamwise location of $x/H = 0$, the maximum standard deviation of the velocity fluctuations within the boundary layer is approximately $0.2U_\infty$, indicating the turbulent state of the upper boundary layer. Similar measurements by Grandemange *et al.* (2013) indicated a maximum standard deviation of $0.35U_\infty$ at the upper edge of the rear face.

The 3-D topology of the mean flow is characterized using the symmetry-enforced double-frame tomo-PIV measurements in figure 3. The 3-D isosurface of zero streamwise velocity (green isosurface) in figure 3(*a*) shows the boundaries of the mean separation
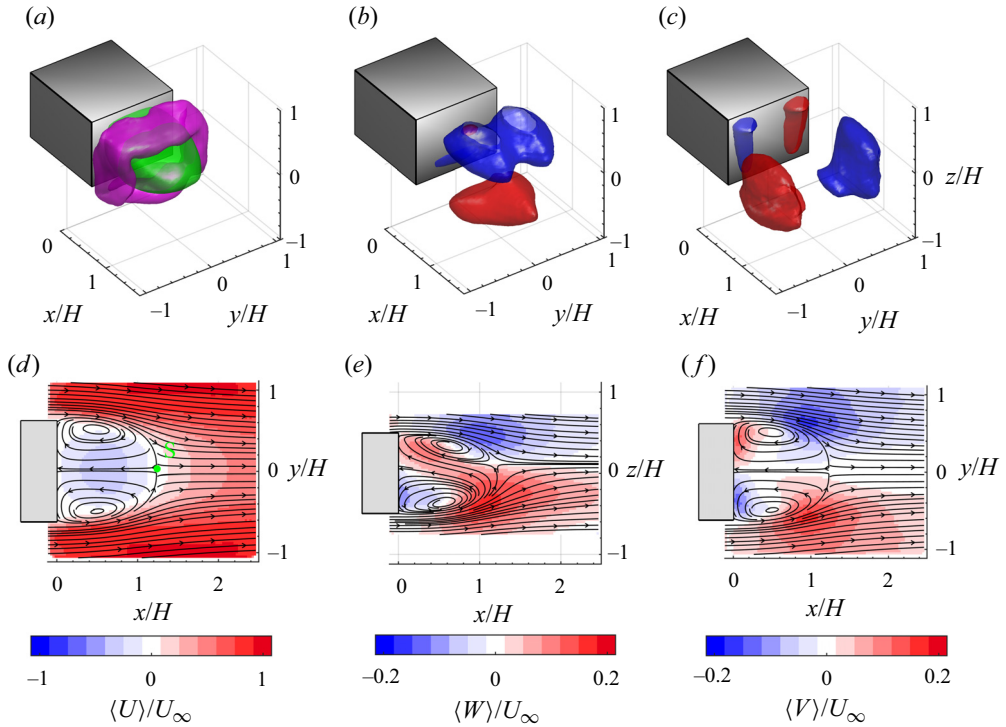
Figure 3. The 3-D and 2-D visualizations of the mean velocity field from tomo-PIV measurements. (*a*) Isosurface of $\langle U \rangle / U_\infty = 0$ (green) and normalized Q-criterion, $QH^2/U_\infty^2 = 0.48$ (purple). (*b*) Isosurfaces of $\langle W \rangle / U_\infty = \pm 0.1$, and (*c*) $\langle V \rangle / U_\infty = \pm 0.1$. Red shows +0.1, and blue shows −0.1. (*d*) Two-dimensional contours of $\langle U \rangle / U_\infty$ at $z/H = 0$ plane, (*e*) contour of $\langle W \rangle / U_\infty$ at $y/H = 0$ and (*f*) contour of $\langle V \rangle / U_\infty$ at $z/H = 0$.

bubble. The main vortical structure of the mean flow is also a toroidal vortex, as seen from the purple isosurface of the Q-criterion (Hunt, Wray & Moin 1988). The 2-D streamlines of figure 3(*d*) in $z/H = 0$ plane show that the two mean recirculation regions are identical, and the saddle point is at $y/H \sim 0.2$, as expected from the averaging of the symmetry-enforced data.

In figure 3(*b*), the negative and positive isosurfaces of $\langle W \rangle / U_\infty$ show different topologies for the isosurfaces of downward and upward flow. The downward flow (blue isosurface) consists of two lobes. The shape indicates that the intense downward motions are on either side of the spanwise centre at $y/H \sim \pm 0.33$. In contrast, the upward flow topology (red isosurface) shows a single triangular-shaped region with the peak of the upward at the spanwise centre. Kang *et al.* (2021) also demonstrated two off-centred downward zones and a strong central upward for an Ahmed body placed in a thick boundary layer. Despite the shape difference, the volume within the displayed isosurfaces of upward and downward is approximately similar. Figure 3(*e*) also shows the upward and downward motions where the streamlines curve around the end of the separation bubble at $x/H \sim 1$. In addition, the recirculation zones generate an upward zone close to the upper edge and a downward zone close to the lower edge of the rear face.

The spatial organization of the two opposing spanwise motions is shown in figures 3(*c*) and 3(*f*). There are small zones of spanwise motion near the rear face in figure 3(*c*), while the larger zones are farther downstream. The zones of spanwise motions are elongated in the z direction and symmetric with respect to the $y/H = 0$ plane. Figure 3(*f*) shows that

985 A19-12

the weaker spanwise motions form upstream of the recirculation zone, while the stronger motions form close to the end of the separation bubble at $x/H \sim 1$.

4. Barycentre of the wake deficit

To evaluate the presence of the bi-stable mode and investigate the oscillations of the separation bubble, the barycentre of the wake deficit is analysed. Unlike previous investigations that calculated the barycentre within 2-D planes (e.g. Grandemange *et al.* 2013; Haffner *et al.* 2020), the current study computes the barycentre using 3-D velocity fields obtained from tomo-PIV measurements. Using the 3-D data, the spanwise barycentre location is calculated following

$$
y_b = \frac{\iiint_{\Omega} y(1 - U/U_{\infty}) \, d\Omega}{\iiint_{\Omega} (1 - U/U_{\infty}) \, d\Omega}.
\tag{4.1}
$$

Here, the integrals are calculated within volume Ω of the wake where $U/U_{\infty} < 1$. A similar equation is used for calculating x_b and z_b.

Figure 4 displays the distributions of the joint probability density function (JPDF) for y_b and z_b. These distributions were obtained from the original three double-frame datasets and ten time-resolved datasets of tomo-PIV measurements in figures 4(*a*) and 4(*b*), respectively. The symmetry-enforced data are not utilized in this figure to allow for the observation of asymmetry present in the original dataset. Figure 4(*a*) shows two high probability y_b locations at $\pm 0.05H$ due to the spanwise bi-stability (Grandemange *et al.* 2013). These y_b/H locations are consistent with the values reported by Grandemange *et al.* (2013) and Fan *et al.* (2020). However, a slight disparity in the magnitudes of the two peaks is observed due to an insufficient statistical convergence resulting from the prolonged duration of each bi-stable state. As expected, the wake only demonstrates one high probability location in the z direction at $z_b/H = -0.03$, indicating no bi-stable motion in the vertical direction. For time-resolved data with shorter overall duration, the asymmetry increases in figure 4(*b*) showing a stronger peak at $y_b = +0.05H$ relative to the peak at $y_b = -0.05H$. Upon inspecting the time-series datasets, it is evident that out of the 10 datasets, y_b maintained a positive value in 8 datasets, was negative in one dataset and switched between positive and negative in the remaining dataset. In terms of duration, y_b was positive in 88 % of the measurement time, and negative in 12 % of the time for the time-resolved data. The asymmetry can be avoided by collecting additional datasets, but the prolonged tomo-PIV data processing prohibited us from collecting additional datasets. As explained in § 2.3, the asymmetry of the data is addressed by creating a symmetry-enforced dataset, achieved through appending the original dataset with a spanwise-flipped copy of the data.

Figure 5(*a*) displays the pre-multiplied power spectral density (PSD) of normalized fluctuations of the barycentre locations (i.e. x_b'/H, y_b'/H, and z_b'/H). These spectra depict both the frequency and magnitude of fluctuations in the separation bubble's position. For calculating the PSD, the time series of barycentre location from each time-resolved tomo-PIV dataset is divided into 3 segments with 50 % overlap and then weighted by a hamming window. Therefore, in total 30 segments, each $73H/U_{\infty}$ long, are used for calculating the PSDs. Note that the analysis of figure 5 is also carried out using the original data without symmetry enforcement since it does not affect the PSDs of figure 5.
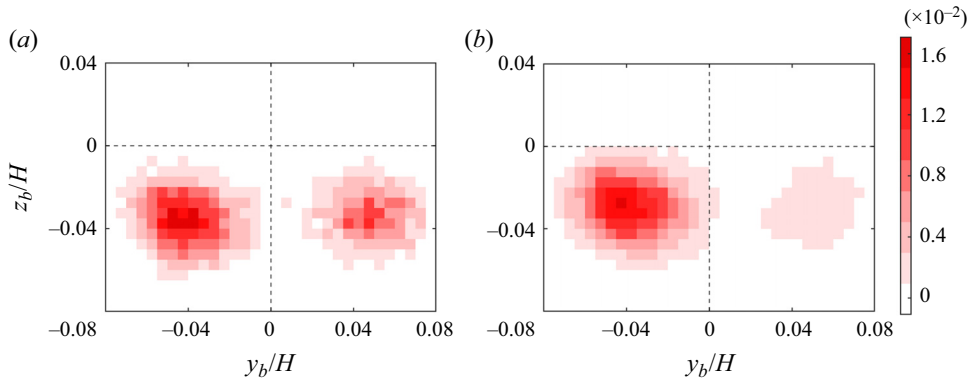
Figure 4. The JPDF of the barycentre of momentum deficits for (*a*) 3 double-frame and (*b*) 10 time-resolved tomo-PIV datasets.
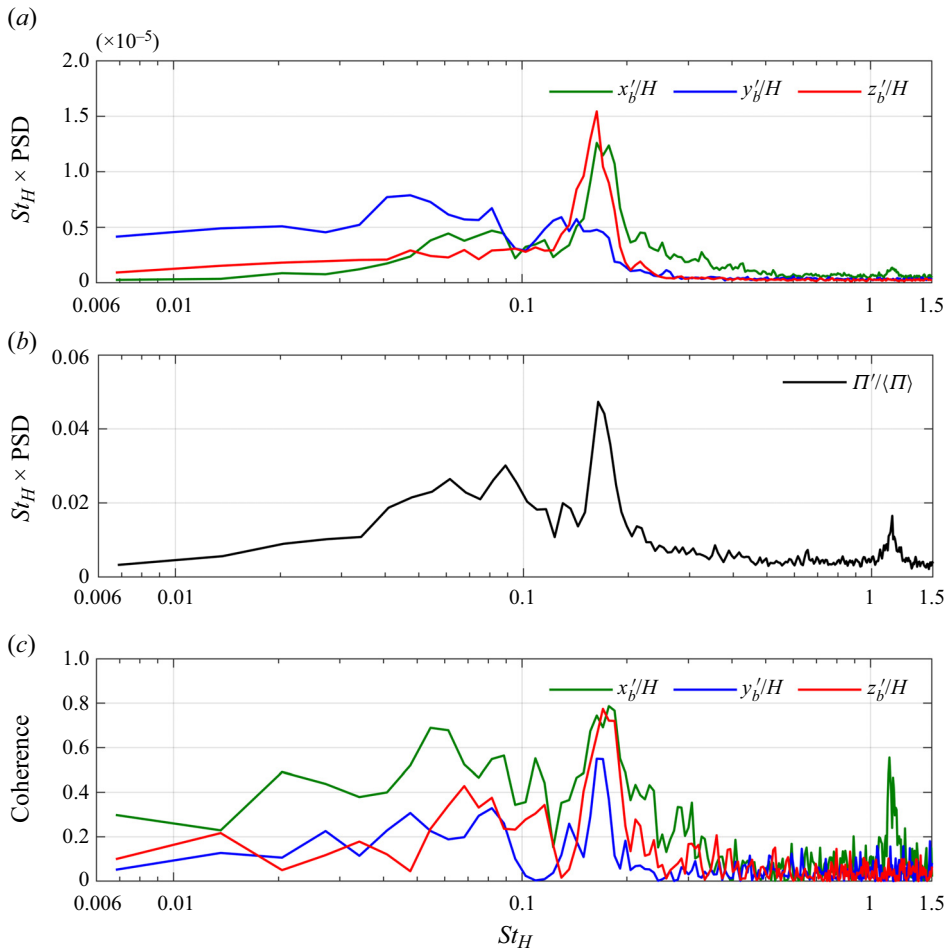

Figure 5. (*a*) The pre-multiplied PSD of the normalized fluctuations in barycentre location $(x'_b/H, y'_b/H, z'_b/H)$, (*b*) the normalized fluctuations in backflow volume, $\Pi'/\langle\Pi\rangle$. (*c*) The coherence function computed between $(x'_b/H, y'_b/H, z'_b/H)$ and $\Pi'/\langle\Pi\rangle$.

985 A19-14

At the low St_H end of the spectrum, the pre-multiplied PSD of y'_b exhibits higher energy levels than that of x'_b and z'_b, possibly due to spanwise bi-stability. The PSD shows two regions of high energy: the first is between St_H values of 0.03 and 0.09, which is similar to the St_H range reported previously for bubble-pumping motion (Duell & George 1999; Khalighi *et al.* 2001; Volpe *et al.* 2015; Dalla Longa *et al.* 2019). However, additional investigation is required to determine if the y'_b fluctuations at this range are due to the bubble-pumping motion. The pre-multiplied PSD of x'_b also displays low-frequency fluctuations between $St_H = 0.05$ and 0.1, but they are less significant than those observed for z'_b. The second region of high energy for y'_b is between St_H values of 0.11 and 0.18 and is attributed to the barycentre oscillations generated by vortex-shedding motion, which is proposed based on its similarity to the St_H value reported for spanwise vortex shedding (Grandemange *et al.* 2013). Similar energetic motions are also observed in the pre-multiplied PSD of x'_b and z'_b, with narrower and stronger peaks. The peak of z'_b occurs at $St_H = 0.16$, which is consistent with vertical vortex shedding observed by Grandemange *et al.* (2013). Finally, a third small peak at St_H of 1.15 is visible in the x'_b fluctuations spectrum.

Figure 5(*b*) presents the pre-multiplied PSD of the fluctuations in the separation bubble's volume. The volume of the separation bubble, Π, is identified where the velocity $U < 0$, and its fluctuations are denoted as Π'. The spectrum exhibits a low St_H zone at $St_H = 0.04$ to 0.1, which is energetically more significant than the low St_H zone observed for y'_b in figure 5(*a*). Haffner *et al.* (2020) investigated the pre-multiplied PSD of the recirculation size based on the streamwise-spanwise cross-sectional area obtained from 2-D-PIV measurements. They found a narrow peak at $St_H = 0.06$, which they attributed to the bubble-pumping mode. The narrower peak in Haffner *et al.* (2020) could be due to the use of 2-D area instead of the 3-D volume used in figure 5(*b*). However, further investigation of the corresponding flow motions is necessary to confirm if the low St_H range observed in figure 5(*b*) is consistent with the bubble-pumping motion. The mid-frequency peak at St_H of 0.15 to 0.19 is in agreement with the vortex-shedding process, which varies the volume of the separation bubble through vortex roll-up. Additionally, the third peak at $St_H = 1.15$ is more pronounced than the peak observed for x'_b in figure 5(*a*). This high St_H motion with smaller energy is attributed to shear layer instabilities mentioned in studies by Duell & George (1999), Khalighi *et al.* (2001) and Haffner *et al.* (2020).

To investigate the correlation between the fluctuations in barycentre location and the separation volume, the coherence function between each coordinate of the barycentre fluctuations (x'_b, y'_b, z'_b) and Π' is shown in figure 5(*c*). The analysis reveals that at the vortex shedding St_H of 0.16, the fluctuations in Π' correlated with the fluctuations of all three coordinate locations x'_b, y'_b and z'_b. Interestingly, the low St_H fluctuations of Π' correlate with the fluctuations in x'_b, whereas it shows a smaller correlation with y'_b and z'_b. At the higher St_H of 1.15, the fluctuations in Π' also only correlated with x'_b.

The results indicate that the fluctuations of Π' at $St_H = 0.04$ to 0.1 are a result of low energy oscillations of the barycentre in the x-direction, consistent with the expected dynamics of the bubble-pumping motion. However, the fluctuations of Π' at the vortex shedding St_H of 0.15 to 0.19 occur along with the barycentre oscillations in all three coordinate directions. Notably, the shear layer instabilities at $St_H = 1.15$ only result in barycentre oscillations in the x-directions, leading to fluctuations of Π'. It's important to note that although the spectral analysis of figure 5 allows us to compare the St_H of these motions with those reported in the literature, it only allows us to speculate about the

mechanism behind them. In § 6, we will demonstrate the dynamics of these motions at each St_H in detail using the SPOD technique.

5. Proper orthogonal decomposition

Several studies have used the POD technique to model and characterize the wake dynamics of an Ahmed body. For instance, Volpe *et al.* (2015) and Pavia *et al.* (2018) employed POD to analyse pressure fluctuations at the rear-face. Pavia *et al.* (2018) also performed POD of stereoscopic PIV measurements at two cross-flow planes. Perry *et al.* (2016*a*), Pavia *et al.* (2020) and Booysen *et al.* (2022) applied POD analysis to 3-D flow measurements. Fan *et al.* (2020) compared the POD analysis of planar PIV measurements with the POD of planar data from a numerical simulation. Podvin *et al.* (2020, 2021) applied POD to a large 3-D domain obtained from direct numerical simulations. To identify similarities and highlight limitations of the POD analysis, the present study briefly compares its results with those of previous investigations.

Figure 6(*a*) shows the energy distribution of the ten leading POD modes. The first mode in the current study contains 9.9 % of the total turbulent kinetic energy, which is smaller than the energy reported in previous studies using 3-D measurements. For example, the first mode contained 15 % of the turbulent kinetic energy in Perry *et al.* (2016*a*), 21 % in Pavia *et al.* (2020) and 33 % in Booysen *et al.* (2022). This discrepancy is likely due to several factors, including the lower Re_H of the current experiment and differences in the duration, domain size and spatial resolution of the measurements. Nevertheless, the energy of the first mode in the current experiment is close to the 8 % energy reported for the lead mode by Podvin *et al.* (2020) at a similar Reynolds number of $Re_H = 10\ 000$. Figure 6(*b*) shows that the remaining POD modes have significantly smaller energy relative to the first mode. Specifically, the second mode contains approximately 1.4 % of the total energy, and the higher-order modes contain an even smaller percentage of the total energy. The large energy difference between the first POD mode and the remaining modes is consistent with previous POD investigations.

The *u*-component of the first POD mode in figure 6(*b*) exhibits two streamwise-elongated structures with opposite signs, resulting in a strong antisymmetry of the wake with respect to the vertical midspan plane of $y = 0$. This mode is known as the spanwise symmetry-breaking mode (Pavia *et al.* 2018). Similar modes have been observed in 3-D POD analyses by Pavia *et al.* (2020), Podvin *et al.* (2020), and Booysen *et al.* (2022). A spanwise antisymmetry has also been observed in the first POD mode of base pressure in Volpe *et al.* (2015) and cross-flow PIV fields in Pavia *et al.* (2018). While Pavia *et al.* (2020) and Podvin *et al.* (2020) attributed the first POD mode to the bi-stability motion, other investigations, including Volpe *et al.* (2015), Pavia *et al.* (2018), and Booysen *et al.* (2022), associated the first POD mode with both bi-stability and spanwise vortex shedding, based on spectral analyses of the mode coefficient.

The second POD mode in figure 6(*c*) consists of two large structures at the upper and lower halves of the wake. The two structures are antisymmetric with respect to the horizontal mid-height plane ($z = 0$). The vertical antisymmetry of this mode resembles the 3-D structures shown in mode 3 of Pavia *et al.* (2020). The third mode in figure 6(*d*) shows two pairs of structures at $x/H \sim 1$ and 2 that are also antisymmetric with respect to the horizontal mid-height plane ($z = 0$) and demonstrates a strong streamwise periodicity. Similar modes with vertical antisymmetry and streamwise periodicity are seen in Fan *et al.* (2020) and Podvin *et al.* (2020). These features are consistent with the spatial characteristics of a vertical vortex-shedding process. Examining the coefficients of modes
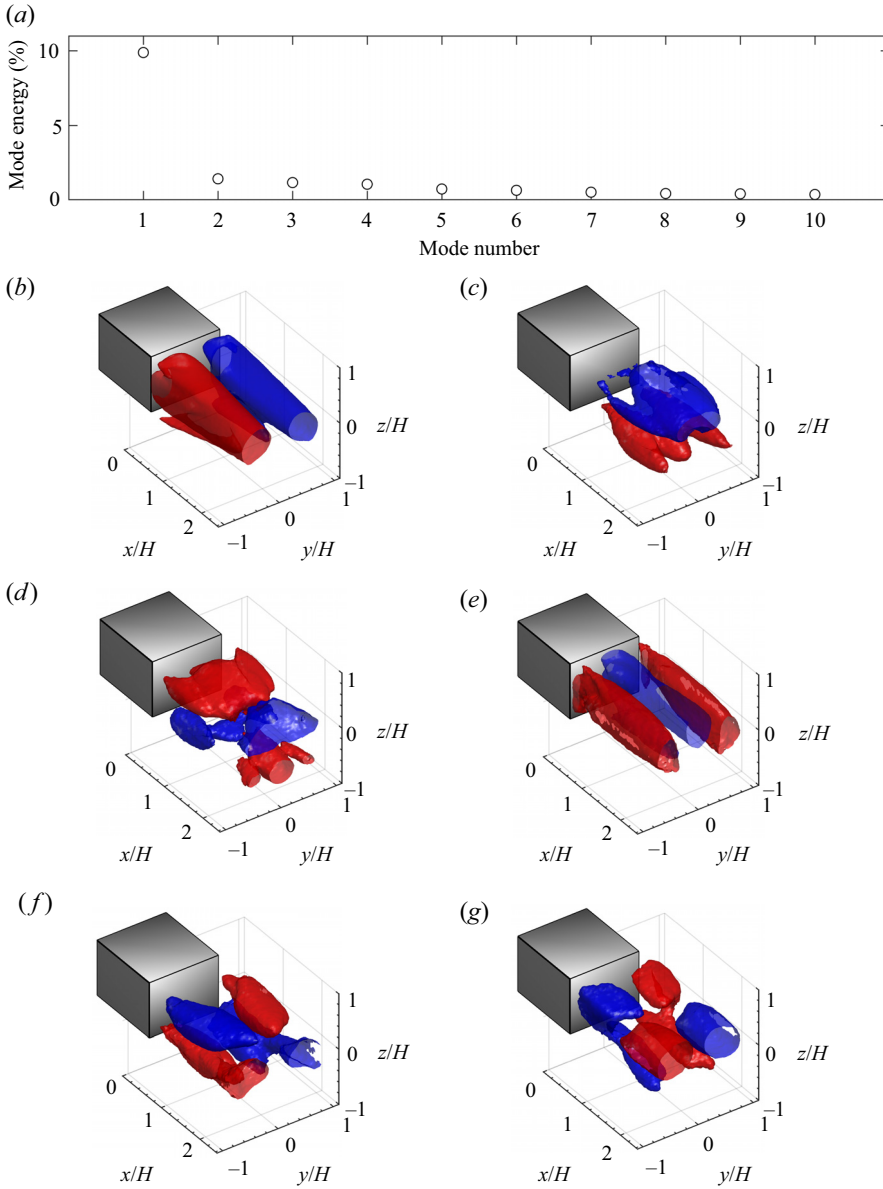
Figure 6. (*a*) Energy of 10 leading POD modes. Panels (*b*) to (*g*) show the spatial structures of the *u*-component for the six leading POD modes ordered from modes 1 to 6, respectively. The red and blue iso-surfaces show similar magnitudes of the streamwise component but with opposite signs.

2 and 3 made it apparent that these two modes undergo oscillations with a consistent phase shift of $\pi/2$, which results in periodic oscillations in the streamwise direction.

Figure 6(*e*) displays the fourth POD mode, which exhibits three large streamwise-elongated structures. Two structures with similar signs are observed at the spanwise sides, while a structure with the opposite sign is located along the mid-span of the wake. This mode exhibits both spanwise and vertical symmetry, as it is symmetric with respect to both the vertical mid-span plane and the horizontal mid-height plane. Previous studies have reported similar symmetry-preserving modes in the POD analysis of base pressure (Volpe

Zone	Flow motion	St_H	1st mode energy (%)	2nd mode energy (%)
A	Bi-stability	<0.014	17.5	6.5
B	Swinging/flapping	$0.014 \leq St_H < 0.123$	14.2	18.6
C	Vortex shedding	$0.123 \leq St_H < 0.234$	31.4	27.3
D	Small-scale structures	$0.234 \leq St_H < 1.024$	16.5	20.5
E	Shear layer instability	$1.024 \leq St_H < 1.228$	2.7	2.4

Table 1. The flow motion, St_H range, and energy percentage of each zone specified in figure 7.

et al. 2015; Pavia *et al.* 2018), planar PIV (Pavia *et al.* 2018; Fan *et al.* 2020), tomo-PIV (Pavia *et al.* 2020), and 3-D-PTV measurements (Booysen *et al.* 2022). Modulating this spatial pattern results in the elongation and shortening of the separation bubble in the streamwise direction, which can be associated with the bubble-pumping motion.

In figure 6(*f*), the fifth POD mode exhibits streamwise structures with alternating signs along the four corners of the base. This mode displays spanwise and vertical antisymmetry, consistent with both spanwise and vertical vortex shedding. Similarly, in figure 6(*g*), mode 6 demonstrates comparable antisymmetry to mode 5, while also exhibiting streamwise periodicity. Analysis of the coefficients of modes 5 and 6 shows that they oscillate with a π/2 offset. Therefore, this pair of spatial modes can contribute to the vortex-shedding process in both spanwise and vertical directions.

Figure 6 displays spatial modes that can be linked to known wake motions. However, the significance of most modes, except for mode 1, is unclear due to their low energy. Furthermore, as noted in the Introduction Section, not every POD mode necessarily corresponds to a coherent structure, meaning there may not be a direct one-to-one relationship between modes and coherent structures. For instance, modes 2 and 3 capture vertical vortex shedding, while modes 5 and 6 capture both vertical and spanwise shedding. As a result, a more rigorous analysis utilizing SPOD is necessary to identify the coherent structures.

6. Spectral proper orthogonal decomposition

Figure 7 displays the spectrum of SPOD eigenvalues after multiplying by St_H for the first 10 SPOD modes. The gap between the energy of the first and second SPOD modes is relatively narrow, and at certain St_H values, the energy of these modes almost overlaps. Integration across the frequency spectrum shows that the first mode constitutes 23.1 % of the total turbulent kinetic energy, while the second mode contributes 15.5 %. The spectra in figure 7 also shows that the energy of the first and second modes is significantly higher than the energy of the remaining higher-order modes. The spectrum shown in figure 7 is divided into five distinct zones, taking into account the spatio-temporal characteristics of the flow motions, which will be elaborated on in the subsequent subsections. Table 1 summarizes the flow motions of these zones, their corresponding St_H range, and their energy percentage. The latter is calculated with respect to the total energy of the first and second mode within $0.007 \leq St_H \leq 10.60$ range.

Zone A corresponds to the bi-stable behaviour observed at $St_H < 0.014$. This motion has a long time scale, which manifests in the lowest St_H range of the spectrum. According to table 1, this zone forms 17.5 % of the first mode energy, and 6.5 % of the second mode energy. However, due to the limited number of spanwise switching of the wake barycentre captured in the 20 time-resolved tomo-PIV datasets, the energy of the bi-stability is
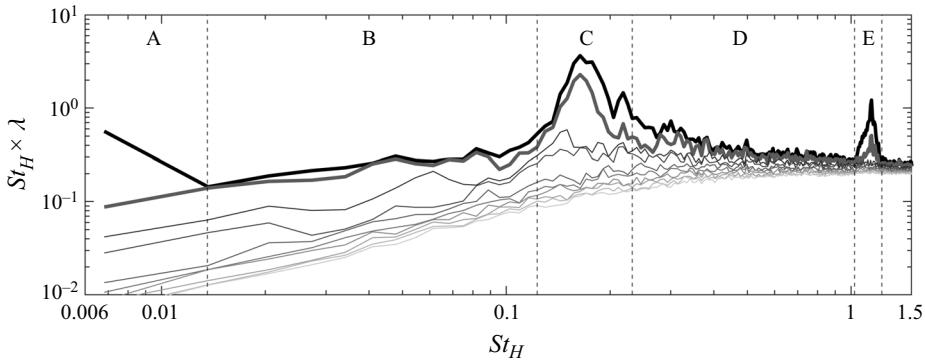
Figure 7. Pre-multiplied spectra of eigenvalues for the first 10 SPOD modes. The thick black and grey lines show the spectra of the first and second SPOD modes, respectively. The remaining thin grey lines indicate the higher-order modes. The frequency domain is divided into five zones as described in table 1.

potentially underestimated. Zone B captures spanwise and vertical swinging/flapping motions of the wake, in the range of $0.014 \leq St_H < 0.123$. Although no major peak is present within this zone, these motions form 14.2 % of the first mode energy and 18.6 % of the second mode energy. Zone C captures vortex-shedding motions in the range of $0.123 \leq St_H < 0.234$. This zone forms 31.4 % of the first mode energy and 27.3 % of the second mode energy. There are two local peaks at $St_H = 0.164$ and 0.218 within zone C. Zone D represents small-scale structures with no apparent spatio-temporal features within $0.234 \leq St_H < 1.024$. The small energy gap between the modes also demonstrates the complexity of flow motions contained in Zone D. Finally, zone E features a peak at $St_H = 1.146$ and is associated with shear layer instability with a small energy contribution. For $St_H \geq 1.228$, no peak can be identified from the pre-multiplied spectrum and the energy gap between the SPOD modes is notably small. The following subsections examine the spatio-temporal characteristics of the first SPOD mode within all the zones, except for zone D, which lacks coherent structures. The spatio-temporal characteristics of the second SPOD mode are also discussed when its energy at any St_H is comparable to that of the first mode.

6.1. *Bi-stable motions*

Figure 8 depicts the spatial organization of the first SPOD mode at $St_H = 0.007$ in zone A. This SPOD mode features two antisymmetric structures that extend the entire streamwise length of the domain, with their axes positioned slightly above the mid-height plane at $z/H \sim 0.2$. In figures 8(*a*) and 8(*c*), smaller and weaker structures are also visible closer to the wall at $z/H \sim -0.4$. The observed symmetry-breaking pattern provides strong evidence of a spanwise asymmetry in the wake that undergoes switching. The *x*-component of the reduced-order model, u_{ROM}, generated using this SPOD at $St_H = 0.007$, can be viewed in supplementary movie 1 available at https://doi.org/10.1017/jfm.2024.288. The movie reveals that the two structures switch signs at phase $\Phi = \pi$ and then revert back to their initial sign at $\Phi = 2\pi$.

The barycentre position during the full cycle of the ROM generated using the SPOD mode at $St_H = 0.007$ is shown in figure 9. The variation of the barycentre in the *y–z* plane is presented in figure 9(*a*), and the variation in the *x–z* plane is shown in figure 9(*b*). The phases of the ROM, when y_b is at the most negative location, zero and the most positive
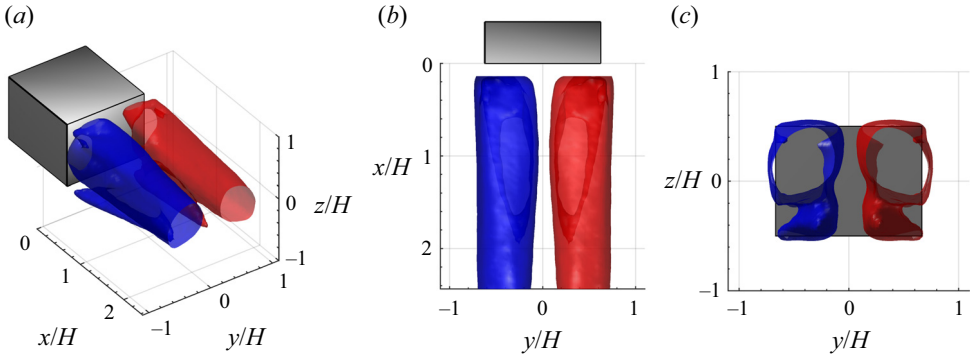
Figure 8. Spatial organization of the first SPOD mode at $St_H = 0.007$ in (*a*) isometric view, (*b*) top view and (*c*) back view. The red and blue isosurfaces show $\Psi_{u,l}/U_\infty = \pm 0.25$ for frequency index $l = 2$.
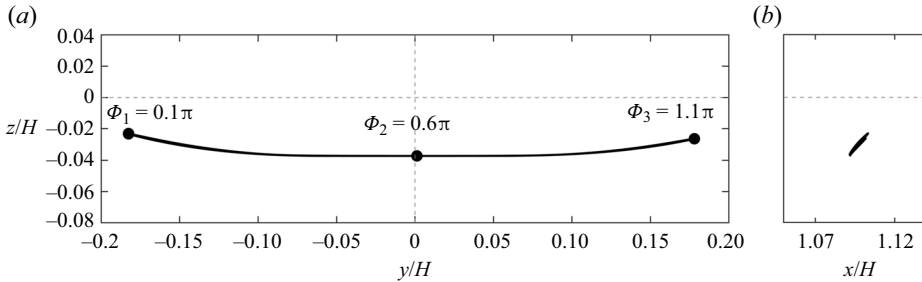

Figure 9. The variations of the wake barycentre based on ROM obtained using the SPOD mode at $St_H = 0.007$. (*a*) The trace of z_b/H versus y_b/H, and (*b*) z_b/H versus x_b/H.

location, are indicated with $\Phi_1 = 0.1\pi$, $\Phi_2 = 0.6\pi$ and $\Phi_3 = 1.1\pi$, as seen in figure 9(*a*). Note that reference phase of $\Phi = 0$ does not have any physical significance and merely acts as a reference point. In other words, a constant value can be subtracted from Φ_1, Φ_2, Φ_3. Although the trace of the barycentre forms a closed loop, it appears as a line because it retraces its own path. Therefore, the trajectory follows a line that slightly moves between $z_b/H \sim -0.04$ and -0.02, consistent with the single most probable z_b/H position observed in figure 4. In contrast, y_b/H varies over a large range from $y_b/H = -0.18$ to 0.18. This variation is larger than the range observed in JPDFs of y_b/H in figure 4. The discrepancy suggests that SPOD modes at other frequencies reduce the range of spanwise motion and the asymmetry caused by the first SPOD mode at $St_H = 0.007$. Moreover, figure 9(*b*) demonstrates that the motion of the barycentre in the x–z plane is negligible. Therefore, the SPOD mode at $St_H = 0.007$ mainly causes the wake to fluctuate in the y-direction, which is consistent with the definition of the bi-stable motion.

Figure 10 provides a visualization of the wake topology of the SPOD mode at $St_H = 0.007$ for Φ_1, Φ_2 and Φ_3 phases. The vortical structures and separation bubble are shown in figure 10(*a–c*), and y–z cross-sections that display the streamlines and mode values are seen in figure 10(*d–f*). To visualize the direction of rotation for streamwise vortices, a modified parameter called Q' is used in conjunction with the Q-criterion. Specifically, Q' was defined as $\omega_x/|\omega_x| \times [QH^2/U_\infty^2]$, where ω_x is streamwise vorticity. Given that Q' has the same absolute value as Q, it identifies vortical structures similar to those identified by Q, but its sign denotes the direction of streamwise vorticity. Specifically,
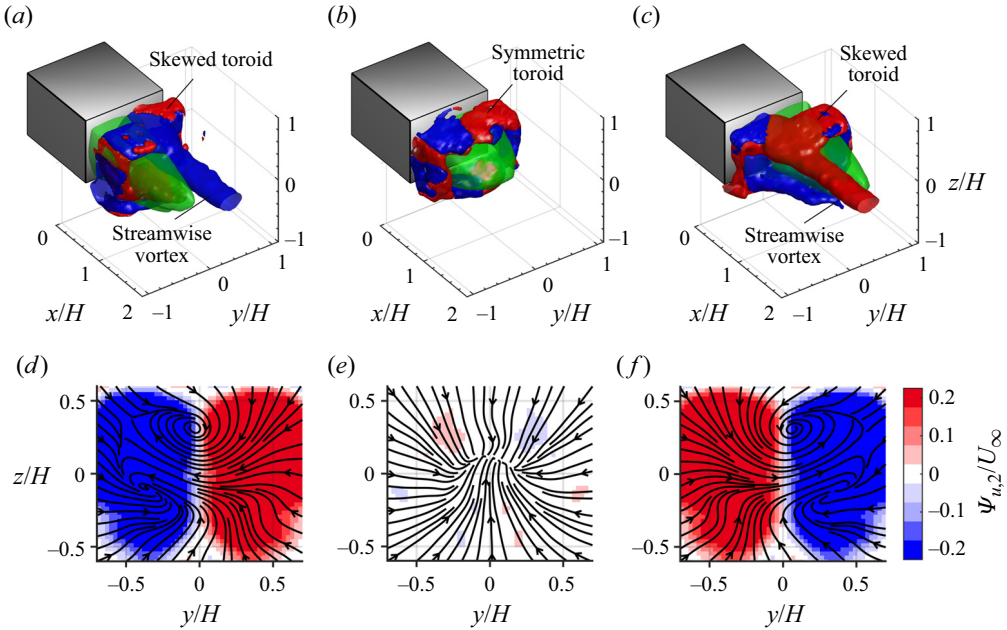
985 A19-20

Figure 10. Visualizations of the ROM reconstructed from the SPOD mode at $St_H = 0.007$ at (a,d) $\Phi_1 = 0.1\pi$, (b,e) $\Phi_2 = 0.6\pi$ and (c,f) $\Phi_3 = 1.1\pi$. In $(a–c)$, the green isosurface shows $U_{ROM} = 0$, red shows $Q' = 0.48$ and blue shows $Q' = -0.48$. In $(d–f)$, 2-D streamlines correspond to V_{ROM} and W_{ROM} components of the ROM, and the contours show u_{ROM} at the cross-flow plane of $x/H = 1.33$.

a positive Q' corresponds to a positive ω_x, whereas a negative Q' corresponds to a negative ω_x.

At $\Phi_1 = 0.1\pi$ in figure 10(a), vortical structures form a toroidal vortex and a streamwise vortex that extend downstream. The streamwise vortex (blue) rotates in a clockwise direction due to its negative ω_x, which is also evident at $(y/H, z/H) = (0, 0.3)$ of the y–z cross-section shown in figure 10(d). This vortex results in a strong spanwise motion in the negative y direction. Inspection of the streamlines in figure 10(d) shows that, in addition to this vortex, there is evidence of a weak counterclockwise vortex at $(y/H, z/H) = (0.3, -0.1)$ that did not appear in the 3-D visualization of figure 10(a). The toroid in figure 10(a) is skewed, with the side at negative y/H shifted in the downstream direction, and the separation bubble tilted towards negative y/H. This asymmetry is consistent with the barycentre location being at the most negative location at Φ_1 in figure 9(a). At $\Phi_2 = 0.6\pi$ in figure 10(b), the wake symmetry is recovered, and the Q' isosurface shows a symmetrical toroid around the separation bubble, with no evidence of strong streamwise vortices. Figure 10(e) shows that the magnitude of the SPOD mode $(\Psi_{u,l})$ is negligible, with the mean velocity dominating the ROM. A stagnation line also appears in the streamlines of figure 10(e). At phase $\Phi_3 = 1.1\pi$, the separation bubble is tilted toward positive y, and a strong streamwise vortex with counterclockwise rotation appears in figure 10(c). Generally, the flow topology at phase Φ_3 is opposite to that of Φ_1, with the separation bubble tilted towards the positive y direction. Supplementary movie 2 provides additional perspectives of the vortical structures and separation bubble at different viewing angles and phases. The top view of the movie clearly shows the streamwise vortex remains at the spanwise centre while changing its rotation direction as the separation bubble shifts from one spanwise side to the other.
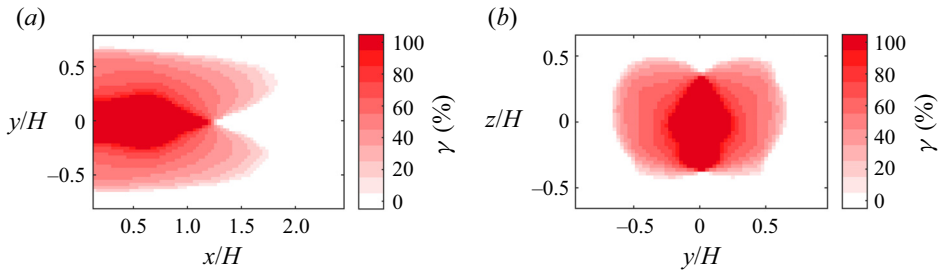
Figure 11. The backflow probability, γ, obtained from U_{ROM} of the first SPOD mode at $St_H = 0.007$ in the (a) $z/H = 0$ and (b) $x/H = 0.5$ planes.

The dynamics of the bi-stable motion shown in figure 10 is relatively consistent with the vortical structures of asymmetric states identified by Pavia *et al.* (2018) using stereoscopic PIV in cross-flow planes, and by Pavia *et al.* (2020) through flow reconstruction using 3-D POD modes. In both investigations, an upper streamwise vortex dominates over a weaker bottom streamwise vortex. Furthermore, Pavia *et al.* (2020) demonstrated that the streamwise vortices originate from the skewed toroid, consistent with visualizations of figure 10. However, according to the numerical studies conducted by Dalla Longa *et al.* (2019) and Fan *et al.* (2020), large hairpin vortices separate from the toroid during the switching of asymmetric states. The SPOD mode at $St_H = 0.007$ does not capture these hairpin vortices. It is plausible that the hairpin shedding is captured by the SPOD mode at higher St_H.

The backflow probabilities, γ, have been calculated using the U_{ROM} of the first SPOD mode at $St_H = 0.007$, and their contours are depicted in figures 11(a) and 11(b) at the $z/H = 0$ and $x/H = 0.5$ planes, respectively. In figure 11(a), the darkest red contour ($\gamma = 100\%$) represents the area that always contains a backward flow, whereas the lightest red contour indicates the maximum extent of the backflow region caused by the oscillations of the bi-stable motion. Notably, the contours demonstrate that the backflow region extends and reaches $x/H = 1.7$ when the wake is skewed in the y direction. Figure 11(b) shows a relatively symmetrical distribution of γ in the cross-flow plane at $x/H = 0.5$ with no bi-stable motion in the vertical direction.

Figure 11(a) shows that the separation bubble length, L_s, is longer for asymmetric states than for the symmetric state. Based on the ROM, the average L_s for the asymmetric states with $y_b \neq 0$ is $1.48H$, longer than the L_s of $1.24H$ for $y_b = 0$ state. This is in agreement with Grandemange *et al.* (2013), who reported the length of the conditionally averaged asymmetric wake is slightly longer than the mean separation bubble length. Grandemange *et al.* (2014) also found that the L_s of a stable asymmetric wake forced by a small rod placed in the wake flow becomes 4 % longer than the L_s of the undisturbed wake. However, the shorter separation bubble length at $y_b = 0$ in figure 11(a) may contradict some findings of Grandemange *et al.* (2014) and Haffner *et al.* (2020). Grandemange *et al.* (2014) generated a stable symmetric wake by placing a small rod along the spanwise centreline of the wake, resulting in an even longer L_s than that of the asymmetric states. Haffner *et al.* (2020) also reported a 2 % longer separation bubble length during wake switching between the two asymmetric states. The apparent discrepancy could be due to the presence of other motions in the symmetric states obtained by Grandemange *et al.* (2014) and Haffner *et al.* (2020) or the method used to obtain the symmetric states in these studies.

Figure 12 demonstrates the impact of the SPOD mode at $St_H = 0.007$ on the separation bubble volume by displaying the fluctuations of the separation volume, Π'_{ROM}, over a
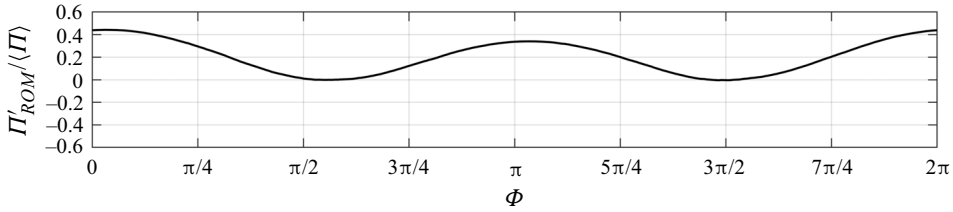
Figure 12. The normalized fluctuations of separation volume $\Pi'/\langle\Pi\rangle$ based on U_{ROM} obtained using the SPOD mode at $St_H = 0.007$.

2π phase duration. Here Π'_{ROM} is calculated as $\Pi_{ROM} - \langle\Pi\rangle$, where $\langle\Pi\rangle$ is the mean separation bubble volume. The figure shows that the volume fluctuations are positive, varying from zero to $0.45\langle\Pi\rangle$. This figure, together with the 3-D visualizations in figure 10, suggests that as the wake tilts in the spanwise direction towards $\Phi_1 = 0.1\pi$ and $\Phi_3 = 1.1\pi$, the separation bubble expands. This is also in agreement with the longer L_s observed in figure 11 during the asymmetric states. The separation bubble returns to a similar size as $\langle\Pi\rangle$ when the wake symmetry is restored at $\Phi_2 = 0.6\pi$. Additionally, figure 12 reveals that the bi-stable motion results in relatively large variations in volume that can reach up to 45 % of $\langle\Pi\rangle$.

6.2. *Swinging/flapping motions*

This section characterizes the SPOD modes within zone B covering the range of $0.014 \leq St_H < 0.123$. Figures 13(*a*)–13(*c*) illustrate a sample of the first SPOD modes at $St_H = 0.034$ from different viewing angles. These modes consist of three streamwise-elongated structures, where the two outer structures have the same sign, while the middle one has an opposite sign. This configuration forms a symmetry-preserving pattern with respect to the $y = 0$ plane. However, there is no symmetry in the vertical direction with respect to the $z = 0$ plane, as evident in figure 13(*c*). An animation of the first SPOD mode at $St_H = 0.034$ is presented in supplementary movie 3. The animation demonstrates that with increasing Φ, the structures move in the vertical direction while always maintaining spanwise symmetry. As the structures move vertically, they are gradually replaced with streamwise structures of opposite sign. The dynamics of this ROM indicates that this mode can only result in vertical and streamwise motions of the separation bubble.

The first SPOD mode at a slightly higher $St_H = 0.041$ is shown in figures 13(*d*)–13(*f*). This mode is visualized here at $\Phi = 0.5\pi$ when the structures are fully extended. In contrast to the previous case, this St_H features only two streamwise-elongated structures that are antisymmetric with respect to the $y = 0$ plane. The structures are similar to the bi-stability mode presented in figure 8. However, considering that the isosurfaces in figure 13 are displayed at $\Psi_{u,l}/U_\infty = \pm 0.08$, a value smaller than the $\Psi_{u,l}/U_\infty = \pm 0.25$ limit in figure 8, it can be concluded that the structures in figure 13 are notably weaker. The ROM of this mode at $St_H = 0.041$ in supplementary movie 4 shows the structures become longer with increasing phase Φ, then gradually fade, and transform to structures with an opposing sign. Smaller and weaker streamwise structures also emerge closer to the wall at $z/H \sim -0.4$ when Φ is approximately 0.5π and 1.5π. Therefore, this mode is anticipated to contribute to spanwise oscillations of the wake, although a smaller displacement is expected compared with those observed for the bi-stability mode at $St_H = 0.007$.
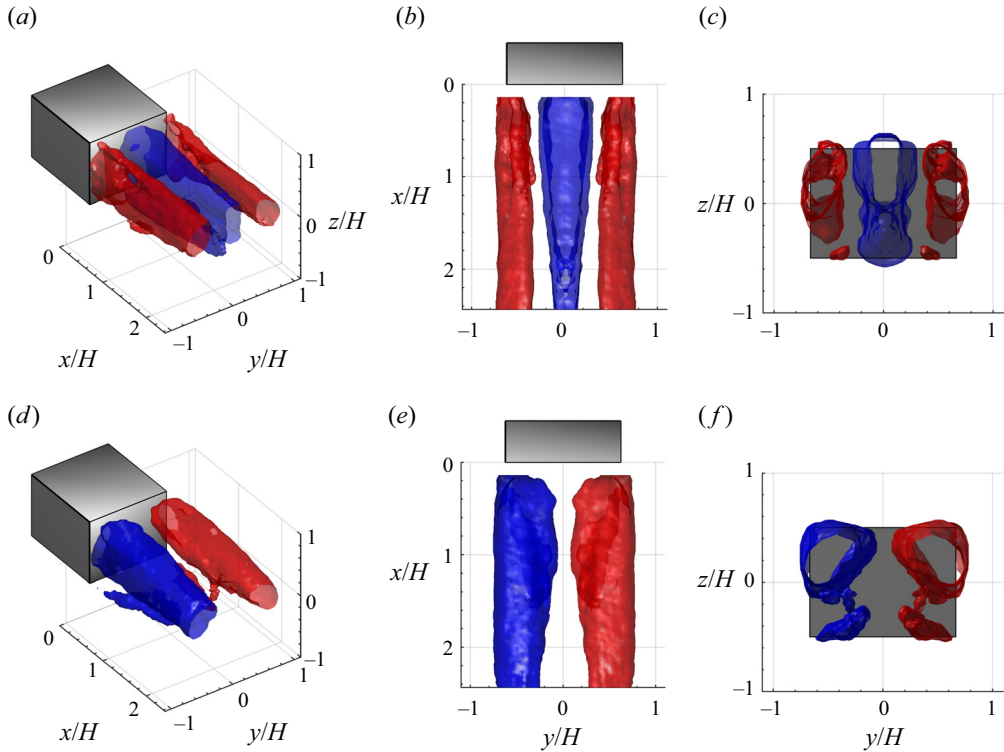
Figure 13. Spatial organization of the first SPOD mode at $St_H = 0.034$ ($l = 6$) in (*a*) isometric view, (*b*) top view and (*c*) back view, and at $St_H = 0.041$ ($l = 7$) in (*d*) isometric view, (*e*) top view and (*f*) back view. The mode at $St_H = 0.041$ is shown at $\Phi = 0.5\pi$. The red and blue isosurfaces show $\Psi_{u,l}/U_\infty = \pm 0.08$.

Examining other first and second SPOD modes within the range of $0.014 \leq St_H < 0.123$ shows either spanwise symmetric structures similar to those in figure 13(*a–c*) or anti-symmetric structures resembling figure 13(*d–f*). Notably, no specific difference is evident between the first and second SPOD modes, as both exhibit either spanwise symmetric or anti-symmetric structures. Moreover, there is no apparent trend with increasing St_H within the $0.014 \leq St_H < 0.123$ range, except for a decrease in strength and therefore irregularity in the visualization of the SPOD modes. In summary, the first and second SPOD modes with $0.014 \leq St_H < 0.123$ all have symmetric or anti-symmetric structures similar to those shown in figure 13.

Figure 14(*a*) shows the trajectory of the barycentre in the *y–z* plane derived from the ROM of the first SPOD mode for all St_H values in the range $0.014 \leq St_H < 0.123$. The trajectory at $St_H = 0.034$ (shown in red) indicates displacements of the barycentre from $z_b/H = -0.06$ to -0.02, with no displacement in the *y* direction. This aligns with the spanwise symmetry observed in the spatial pattern of figure 13(*a–c*) and supplementary movie 3. For future reference, the phases of the ROM, when the trajectory is at the most negative, zero and most positive z_b/H, are labelled in figure 14 as $\Phi_3 = 1.5\pi$, $\Phi_2 = \pi$ and $\Phi_1 = 0.5\pi$ (in red font). In contrast, the barycentre trajectory for $St_H = 0.041$ (shown in black) results in a spanwise motion with no displacement in the vertical direction. Although this barycentre motion is similar to the bi-stability mode in figure 9, the range of motion spans from $y/H = -0.05$ to 0.05, which is 3.5 times smaller than the spanwise displacement of the bi-stability. The phases of the ROM for the $St_H = 0.041$ case, when the
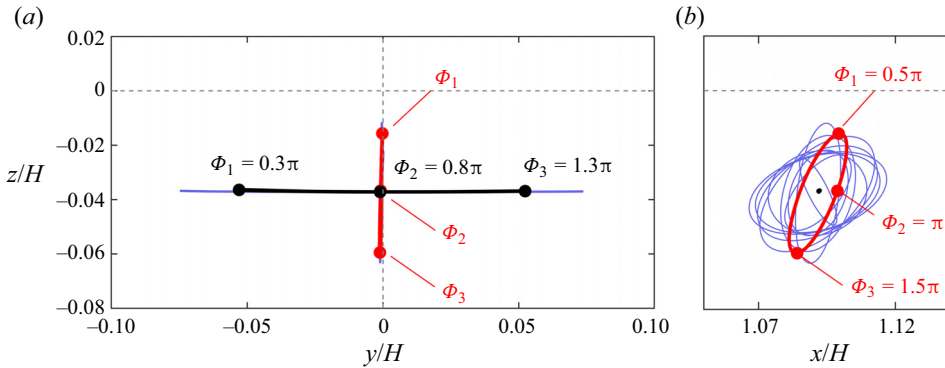
985 A19-24

(*a*)

(*b*)

Figure 14. The trajectory of the wake barycentre projected in the (*a*) *y*–*z* and (*b*) *x*–*z* planes obtained from U_{ROM} for each St_H within $0.014 \leq St_H < 0.123$ range. The red and black lines correspond to the first SPOD modes at $St_H = 0.034$ and 0.041, respectively. The trajectories for the remaining St_H values of the first SPOD mode are shown in blue.

trajectory is at the most negative, zero and most positive y_b/H, are labelled in figure 14(*a*) as $\Phi_1 = 0.3\pi$, $\Phi_2 = 0.8\pi$ and $\Phi_3 = 1.3\pi$.

The trajectories of the remaining St_H values for the first SPOD mode also exhibit similar vertical or horizontal motions of the barycentre in the *y*–*z* plane. However, these trajectories (blue lines) are not distinctly visible in figure 14(*a*) as they are obscured by the red and black lines representing the trajectory of the first SPOD mode at $St_H = 0.034$ and 0.041. Inspection of the trajectories resulting from the second SPOD mode also shows vertical or horizontal motions and are consequently not shown here for brevity.

The trajectories shown in figure 14(*b*) within the *x*–*z* plane show two types of trajectories: elliptical paths involving both vertical and streamwise motions, and a stationary point with no motion in the streamwise or vertical direction. Due to the presence of vertical displacement, the elliptical paths correspond to the symmetry-preserving modes such as the one at $St_H = 0.034$. In contrast, the stationary points correspond to the symmetry-breaking modes such as the one at $St_H = 0.041$ with only spanwise motions. For the elliptical paths the streamwise translations have a similar range as the translations observed in the vertical direction. Examining the trajectories of the second mode (not shown) demonstrates no difference from those of the first SPOD mode in the *x*–*z* plane.

To investigate the spanwise motions, the flow filed reconstructed using the SPOD mode at $St_H = 0.041$ at Φ_1, Φ_2 and Φ_3 is presented in figure 15. The top visualizations of the figure show 3-D vortical structures and the separation bubble, while the lower figures present 2-D contours of streamwise mode magnitude ($\Psi_{u,l}$) and streamlines in $x/H = 1.33$ plane. The vortical structures are visualized using normalized *Q*-criterion defined as $Q^* = QH^2/U_\infty 2$. At Φ_1, as shown in figure 15(*a*), the separation bubble is slightly skewed towards the negative *y* direction, and the toroidal vortex is tilted away from the negative *y* side of the rear-face. The 2-D streamlines of figure 15(*d*) show a node that is skewed towards the region of blue isocontour, indicating a greater momentum deficits. In contrast, the reconstructed flow at Φ_2 in figure 15(*b*) shows a symmetric separation bubble and toroidal vortex. Inspection of the 2-D streamlines in figure 15(*e*) reveals that the node is close to the centre of the *y*–*z* plane. At Φ_3 in figure 15(*c*), the separation bubble and the toroidal vortex are skewed towards positive *y*, showing a pattern opposite to figure 15(*a*). The node is also displaced towards positive *y* as seen in figure 15(*f*). Supplementary movie 5 provides an animation that corresponds to the flow reconstruction shown in figure 15.
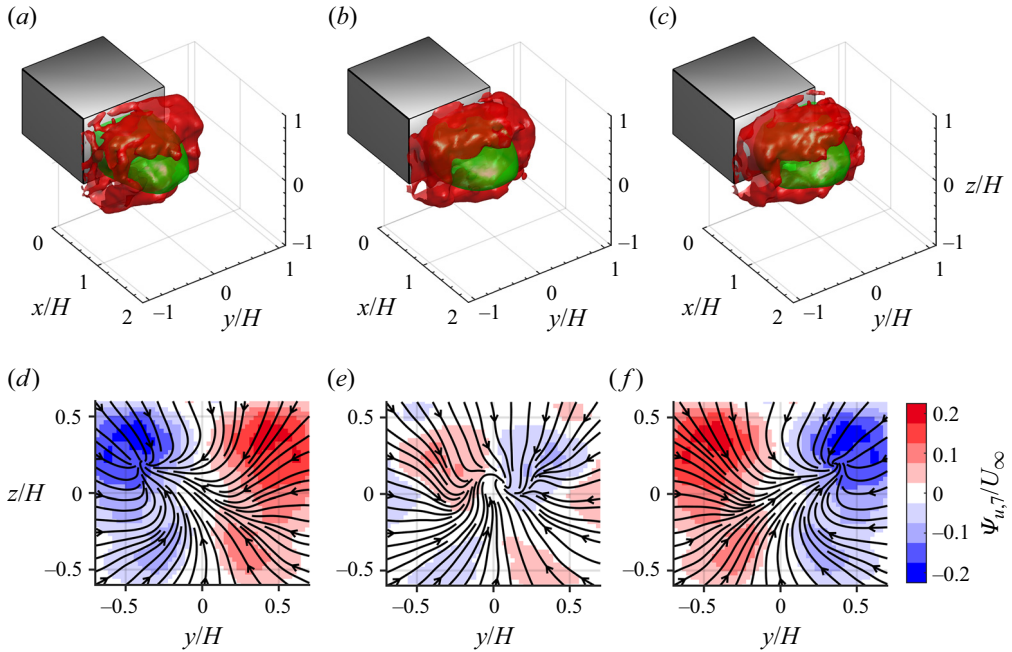
Figure 15. Visualizations of the ROM reconstructed from the SPOD mode at $St_H = 0.041$ at (a,d) $\Phi_1 = 0.3\pi$, (b,e) $\Phi_2 = 0.8\pi$ and (c,f) $\Phi_3 = 1.3\pi$. In $(a–c)$, the green isosurface shows $U_{ROM} = 0$, red shows $Q* = 0.24$. In $(d–f)$, 2-D streamlines correspond to V and W components of the ROM, and the contours show u_{ROM} for $l = 7$ at the cross-flow plane of $x/H = 1.33$.

The animation demonstrates that as Φ increases, the separation bubble and the toroid oscillate between two skewed states. While the toroidal vortex and the separation bubble appears similar to that of the bi-stability in figure 10, a streamwise vortex is not present in the ROM of figure 15 and supplementary movie 5. Therefore, it is concluded that the absence of the streamwise vortex leads to a smaller spanwise motion of the barycentre compared with the spanwise displacement observed in the bi-stability motion.

For brevity, the flow field reconstructed using the first SPOD mode at $St_H = 0.034$ is only depicted in supplementary movie 6. This movie shows vortical structures using Q' (in red and blue), while the separation bubble is visualized in green. The movie shows a toroidal vortex that undergoes deformation and slightly protrudes in the downstream direction with increasing Φ. Additionally, the movie illustrates two weak counter-rotating streamwise vortices emerging at $\Phi = \pi$. At this phase, the top view reveals the separation bubble extending downstream, reaching its maximum length. Subsequently, as Φ increases, the separation bubble contracts, attaining its minimum length at $\Phi = 2\pi$. This motion resembles the expansion and contraction characteristic of the bubble-pumping motion, although the streamwise displacement is small, as seen in figure 14(b). According to the observed barycentre trajectory in figure 14(b) for $St_H = 0.034$ (the red line), the outward motion of the barycentre in the streamwise direction $(+x)$ occurs along with its upward movement $(+z)$. Conversely, the inward streamwise motion $(-x)$ is coupled with a downward motion $(-z)$ of the barycentre.

The probability of backflow based on the U_{ROM} of SPOD mode at $St_H = 0.041$ is depicted in figure 16 for $x–y$ and $y–z$ cross-sections. Overall, the figure shows that the displacements of the backflow region are relatively small, and the edge of the backflow

985 A19-26

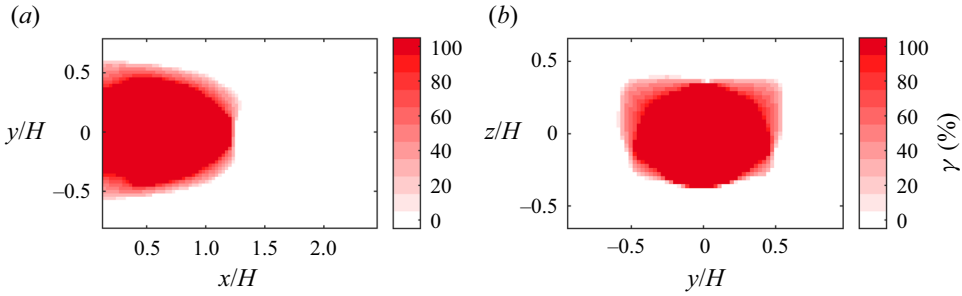(*a*)   (*b*)

Figure 16. Backflow probabilities from U_{ROM} of the SPOD mode at $St_H = 0.041$ in (*a*) $z/H = 0$ and (*b*) $x/H = 0.5$ planes.
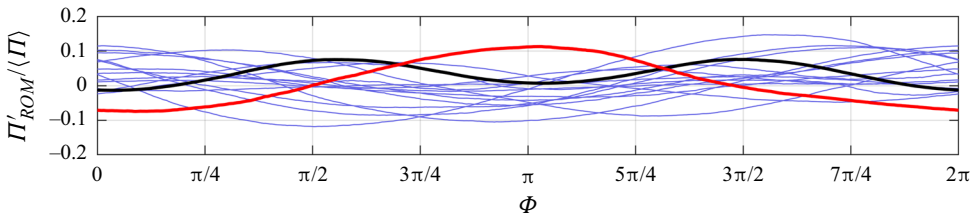

Figure 17. The normalized fluctuations of separation volume $\Pi'/\langle\Pi\rangle$ obtained from U_{ROM} of the first SPOD mode for each St_H within $0.014 \leq St_H < 0.123$ range. The red and black lines indicate the U_{ROM} for $St_H = 0.034$ and 0.041, respectively, while the blue lines correspond to the other St_H values.

region does not oscillate considerably. The transition from $\gamma = 100\,\%$ (red) to $\gamma = 0$ (white) occurs over a short length of approximately $0.1H$ across the spanwise edge of the separation bubble. Therefore, the effect of the first SPOD mode at $St_H = 0.041$ on the spanwise motion of the separation bubble is negligible compared with the bi-stable mode shown in figure 11.

Figure 17 presents the variations in recirculation volume obtained from ROM for each St_H of the first SPOD mode within the range of $0.014 \leq St_H < 0.123$. Thin blue lines represent all St_H cases, except for $St_H = 0.034$ and 0.041, which are illustrated with red and black lines, respectively. The figure shows that the separation volume approximately fluctuates in the range $\pm 0.1 \langle\Pi\rangle$, which is significantly smaller than the variations observed due to the bi-stability motion in figure 12. The variation of Π' can also become negative for $St_H = 0.034$, which involves vertical barycentre translation, in contrast to the positive Π' observed in figure 12. The figure also shows that the Π' variation for $St_H = 0.034$ is slightly larger than Π' variation for $St_H = 0.041$, characterized by spanwise translation of the barycentre. In general, the results indicate that the motions within $0.123 \leq St_H < 0.212$ result in small the expansion and contraction of the separation bubble.

The variations for $St_H = 0.041$ demonstrate that Π' reaches maximum and minimum values at approximately $\Phi = 0.6\pi$ and 1.05π, respectively, closely aligning with the asymmetric states observed in figures 15(*a*) and 15(*c*) at $\Phi_1 = 0.5\pi$ and $\Phi_3 = 1.3\pi$. The midpoint between these extrema in figure 17 also approximately coincides with the symmetric state at $\Phi_2 = 0.8\pi$ in figure 15(*b*). For $St_H = 0.034$, the maximum and minimum Π' occur at $\Phi = \pi$ and 0, respectively. Upon inspecting the top view in supplementary movie 6, it becomes clear that these phase values correspond to the longest and shortest separation bubbles, indicative of the maximum and minimum separation volume. This observation leads to two conclusions when revisiting figures 14 and 5. First,

examination of phase values in figure 14(*b*) reveals that the maximum and minimum volumes at $\Phi = \pi$ and 0 do not align with the barycentre's maximum and minimum z locations (top and bottom points of the trajectory). In fact, the maximum and minimum volumes correspond to the barycentre being at maximum and minimum x locations when the barycentre crosses $z = 0$. Second, the correlation between volume fluctuations (Π') and the coordinates of the barycentre in figure 5(*c*) indicates that Π' fluctuations within $0.014 \le St_H < 0.123$ range mainly corresponds to the streamwise oscillations of the wake barycentre. This indicates that the primary cause of volume oscillations is the streamwise motions of the barycentre due to the vertical swinging motion.

The SPOD analysis showed flow motions within the range of $0.014 \le St_H < 0.123$ result in a small vertical or spanwise movement of the barycentre. The vertical motions were caused by a symmetry-preserving SPOD mode while the spanwise motions were generated by a symmetry-breaking SPOD mode. Both vertical and spanwise motions are referred to as swinging (or flapping) motions here, using the terminology introduced by Pavia (2019) and Pavia *et al.* (2020) to describe movements of the separation bubble that are unrelated to bi-stability motion. The spanwise swinging differs from spanwise bi-stability, as the range of the spanwise motion of the wake barycentre during the swings is several times smaller than the range of spanwise motions of the barycentre induced by the bi-stability. Additionally, visualizations of the flow structures using ROM revealed that the asymmetric state of the swinging motions comprises solely a skewed toroidal vortex, lacking any strong streamwise vortex that was observed in the asymmetric state of the bi-stability motion.

The investigated swinging motions in this study includes the St_H range of 0.04 to 0.08, a range previously associated with bubble-pumping motion in studies by Duell & George (1999), Khalighi *et al.* (2001), Volpe *et al.* (2015) and Pavia *et al.* (2018). The current investigation shows that vertical swinging motions lead to streamwise displacements of the barycentre and variations in the separation bubble volume, aligning with the definition of bubble-pumping motion. However, it is important to note that the change in the separation bubble volume is relatively small, constituting only approximately 10 % of the mean separation bubble volume. Similarly, spanwise swinging motions result in a comparable variation in separation volume, even in the absence of any streamwise motion of the barycentre. Furthermore, the expected in-phase fluctuations around the rear face of the Ahmed body, characteristic of the original bubble-pumping motions, are not apparent in the ROM presented in movie 6. Instead, the in-phase pressure fluctuations noted by Duell & George (1999) at the two spanwise sides of the rear face align with the dynamics of the spanwise-symmetric SPOD mode at $St_H = 0.034$. Consequently, a limited version of the bubble-pumping motion, defined as a small contraction and expansion of the separation bubble and in-phase fluctuations only at the spanwise sides of the rear face, is consistent with the vertical swinging motions observed in the St_H range of 0.014 to 0.123. However, the term swinging/flapping motion describes the key feature of the SPOD motions within this St_H range, specifically referring to the vertical and spanwise motions of the barycentre.

6.3. *Vortex shedding*

This section investigates the SPOD mode for a range of $0.123 \le St_H < 0.234$, corresponding to zone C. Within this zone, the distinguishing characteristic of the SPOD mode is the manifestation of multiple alternating structures in the streamwise direction. These alternating structures, which exhibit opposite signs in the SPOD modes, result in vortex-shedding behaviour. The ROMs of the flow provide further confirmation of this,
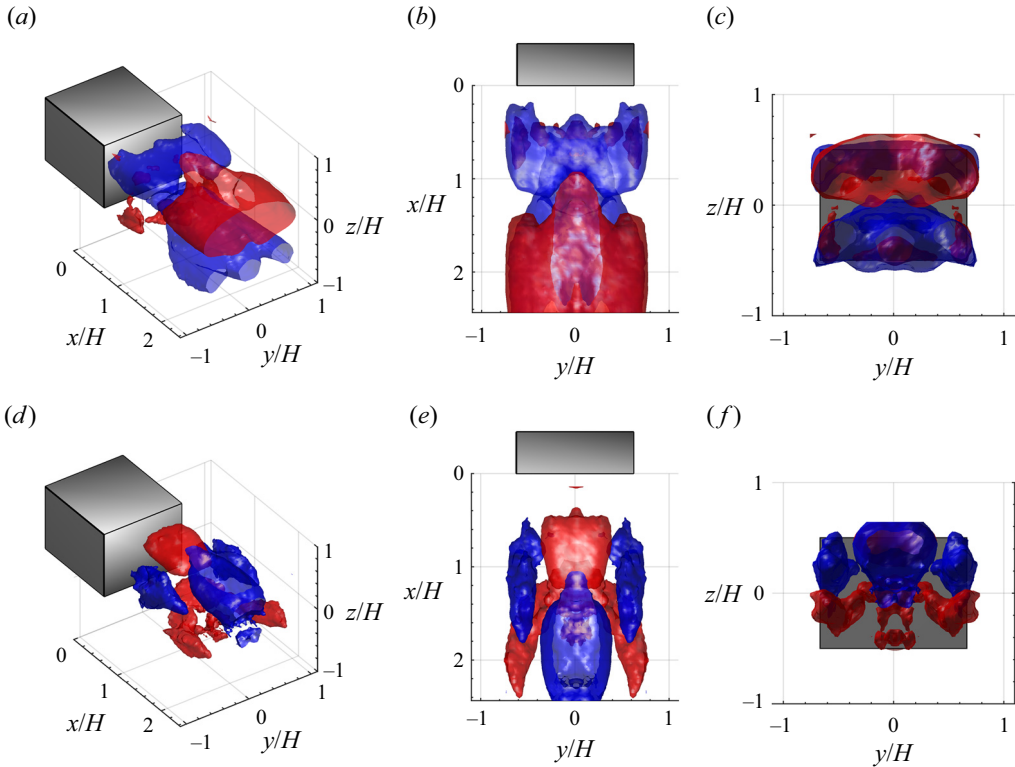
Figure 18. Visualization of the first SPOD mode at $St_H = 0.164$ ($l = 25$) in (a) isometric view, (b) top view and (c) back view, and at $St_H = 0.218$ ($l = 33$) in (d) isometric view, (e) top view and (f) back view. The red and blue isosurfaces show $\Psi_{u,l}/U_\infty = \pm 0.08$ for $l = 25$ and $\Psi_{u,l}/U_\infty = \pm 0.05$ for $l = 33$.

revealing the presence of large vortical structures that are shed downstream. Such unique features set these structures apart from those observed in other zones.

In figure 18(a–c), the SPOD mode for a sample $St_H = 0.164$ is displayed from different viewing angles. This St_H corresponds to the high energy peak seen in the eigenvalue spectrum of figure 7. The SPOD mode displays a pair of structures with opposite signs arranged vertically at the downstream region of the measurement domain. Another pair of smaller structures with opposite signs is also observed closer to the rear face of the Ahmed body. This spatial arrangement bears a resemblance to the third POD mode in figure 6(d), which was attributed to the vertical vortex shedding. The structures of figure 18(a–c) exhibit spanwise symmetry, consistent with utilizing symmetry-enforced data. They also demonstrate an approximate anti-symmetry in the vertical direction with respect to $z = 0$ plane as seen in figure 18(c). The animation of this SPOD mode is available in supplementary movie 7, showing streamwise advection of pairs of structures with alternating sign. The movie also shows that the structures within each vertical pair are not precisely identical, exhibiting a slight deviation from vertical anti-symmetry.

A visualization of the first SPOD mode corresponding to the smaller peak of the pre-multiplied spectra of eigenvalues in figure 7 at $St_H = 0.218$ is presented in figure 18(d–f). This visualization also shows vertical pairs of structures with alternating signs that possess spanwise symmetry. However, the structures of each pair are significantly dissimilar; the downstream pair consists of an ellipsoidal structure at the spanwise centre (in blue), while its lower counterpart consists of an arch-shaped structure
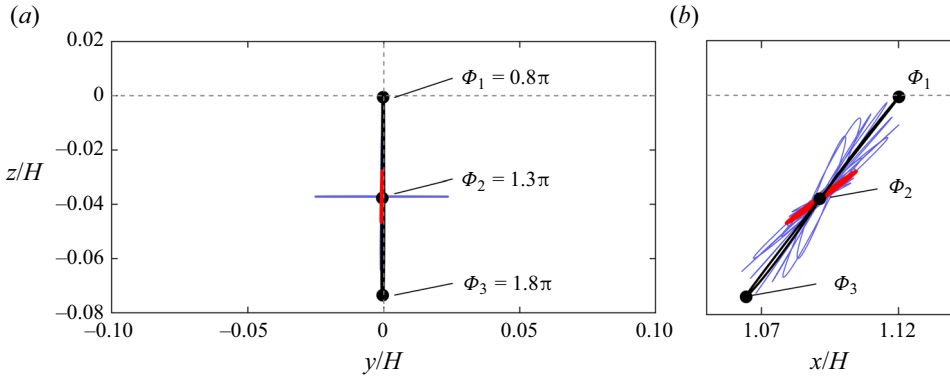
Figure 19. The trajectory of the wake barycentre in the (*a*) *y*–*z* and (*b*) *x*–*y* planes. The coordinates of the barycentre (x_b, y_b, z_b) are obtained from U_{ROM} of the first SPOD mode for each St_H within $0.123 \leq St_H < 0.234$. The black and red lines indicate the U_{ROM} for $St_H = 0.164$ and 0.218. Blue lines show the trace of the remaining St_H values.

(in red). Consequently, there is no antisymmetry in the vertical direction. Nevertheless, the visualization in supplementary movie 8 shows that these structures also advect in the streamwise direction, thus they correspond to the vortex-shedding category.

The barycentre trajectory from the ROM of the modes within the $0.123 \leq St_H < 0.234$ range is depicted in figure 19. All trajectories are represented by thin blue lines, except for $St_H = 0.164$ and 0.218, which are shown with a thick black and red lines, respectively. The barycentre motions for $St_H = 0.164$ and 0.218 follow a vertical trajectory in the *y*–*z* plane and an oblique trajectory in the *z*–*x* plane. Note that many vertical trajectories in the *y*–*z* plane are not visible as they are obscured by the thicker black and red lines. This applies to the trajectories for most St_H values, except for a few cases that demonstrate solely spanwise motion in the *y*–*z* plane. In these instances, the trajectory in the *x*–*z* plane forms a point. Generally, the range of motions is greater in the *z*-direction compared with the *x*-direction, with the smallest range observed in the *y*-direction. This order is in line with the magnitudes of spectral peaks observed at $St_H = 0.16$ in figure 5(*a*), showing a larger peak for z'_b, followed by x'_b, and finally y'_b. Overall, the unique feature of trajectories for zone C is the oblique motion of the barycentre in the *x*–*z* plane that moves the barycentre upwards and away from the wall, then downwards and closer to the rear face. Therefore, the barycentre motions generated by the vortex-shedding motions are distinct from those caused by bi-stability and swirling motions.

Figure 20 shows the spatial organization of vortical structures at three selected phases of the ROM reconstructed using the SPOD mode at $St_H = 0.164$. These three phases, Φ_1, Φ_2 and Φ_3, are indicated on the barycentre trajectory in figure 19. At $\Phi_1 = 0.8\pi$, figure 20(*a*) displays two counter-rotating quasi-streamwise vortices that are connected to the toroidal vortex and extended outwards in the downstream direction. Examination of supplementary movie 9 reveals that these two vortices initiate from the inner-bound of the toroid and divert outwards in the spanwise direction. Consequently, they have vorticity components in both the *x* and *y* directions. These quasi-streamwise vortices move downstream and out of the measurement domain with increasing Φ. At $\Phi_2 = 1.3\pi$, only the tail of these vortices is visible in the downstream region of figure 20(*b*) and new streamwise vortices start forming at the toroidal vortex. As the phase increases to $\Phi_3 = 1.8\pi$, the new pair of quasi-streamwise vortices with an opposite direction of rotation have extended from the toroid as seen in figure 20(*c*). The new vortex pair extends in the downstream direction,
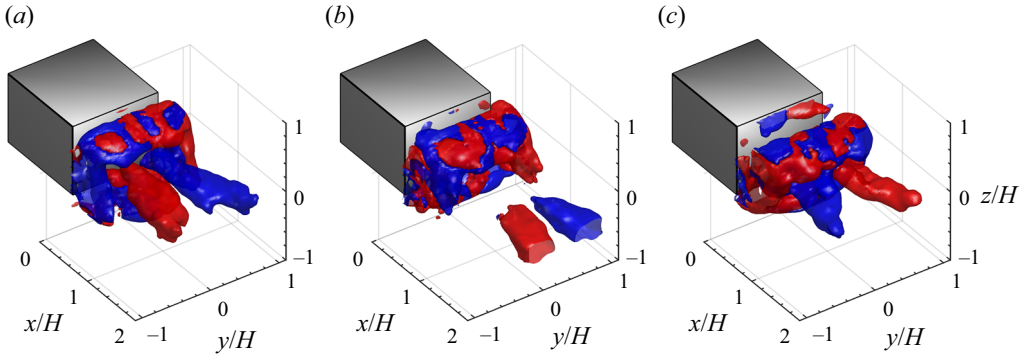
985 A19-30

Figure 20. Visualizations of ROM reconstructed from the first SPOD mode at $St_H = 0.164$ at (a) $\Phi_1 = 0.8\pi$, (b) $\Phi_2 = 1.3\pi$ and (c) $\Phi_3 = 1.8\pi$. The red isosurface shows $Q' = +0.52$, and blue shows $Q' = -0.52$.

and their rotation is opposite to those observed at Φ_1. Additionally, supplementary movie 9 shows that the streamwise vortices arise from the inner part of the toroidal vortex.

For brevity, the spatial organization of vortical structures for the SPOD mode at $St_H = 0.218$ is only shown in supplementary movie 10. The visualization resembles the spatial organization observed at $St_H = 0.164$, demonstrating quasi-streamwise vortices moving in the downstream direction. Upon analysing other St_H values within zone C, the results indicate that the shedding process primarily involves quasi-streamwise vortices. Therefore, an important observation is that the shedding process mainly consists of quasi-streamwise vortices.

To demonstrate how vortex-shedding results in velocity fluctuations, figure 21 illustrates v_{ROM} and w_{ROM} of the SPOD mode at $St_H = 0.164$. The reconstructions correspond to the three selected phases, Φ_1, Φ_2 and Φ_3. At $\Phi_1 = 0.8\pi$ in figure 21(a), the velocity field displays two large zones of upward and downward velocity fluctuations along the centreline. The two quasi-streamwise vortices seen in figure 20(a) generate the Y-shaped upward velocity region (in green) in their outer boundary, while they induce a combined zone of downward velocity between them (in blue). These vortices also generate strong spanwise motions in both the positive and negative y directions, as seen in figure 21(d). The vertical and spanwise motions persist and advect downstream, as seen at $\Phi_2 = 1.3\pi$ in figures 21(b) and 21(e). Similarly, figures 21(c) and 21(f), corresponding to $\Phi_3 = 1.8\pi$, show similar structures as Φ_1 but with opposite magnitudes, consistent with the reversal of the direction of rotation of the vortices in figure 20(c). Vertical and spanwise velocity fluctuations for the SPOD mode at $St_H = 0.218$ exhibit patterns similar to those shown in figure 21. The corresponding figures are not shown for brevity.

Figure 22 illustrates the variations of the separation bubble volume for all St_H values of zone C. All trajectories are shown with thin blue lines except for $St_H = 0.164$ and 0.218, which are shown in black and red, respectively. The ROM shows that Π' for $St_H = 0.164$ varies between minimum and maximum values of $-0.07\langle \Pi \rangle$ and $+0.13\langle \Pi \rangle$ occurring at $\Phi = 0.8\pi$ and 1.6π, respectively. The minimum Π' corresponds to the moment shown in figure 20(a), wherein the streamwise vortices have reached full extension and are still connected to the toroidal vortex. As illustrated in figure 21(a), these vortices generate a strong upward motion in the positive z-direction. At $\Phi = 1.6\pi$ of the maximum Π', as demonstrated in supplementary movie 9, new quasi-streamwise vortices are formed, although not fully extended. However, due to their opposite rotation direction, these vortices induce a downward motion in the z-direction. This observation aligns with the oblique barycentre trajectory illustrated in figure 19(b), where the separation
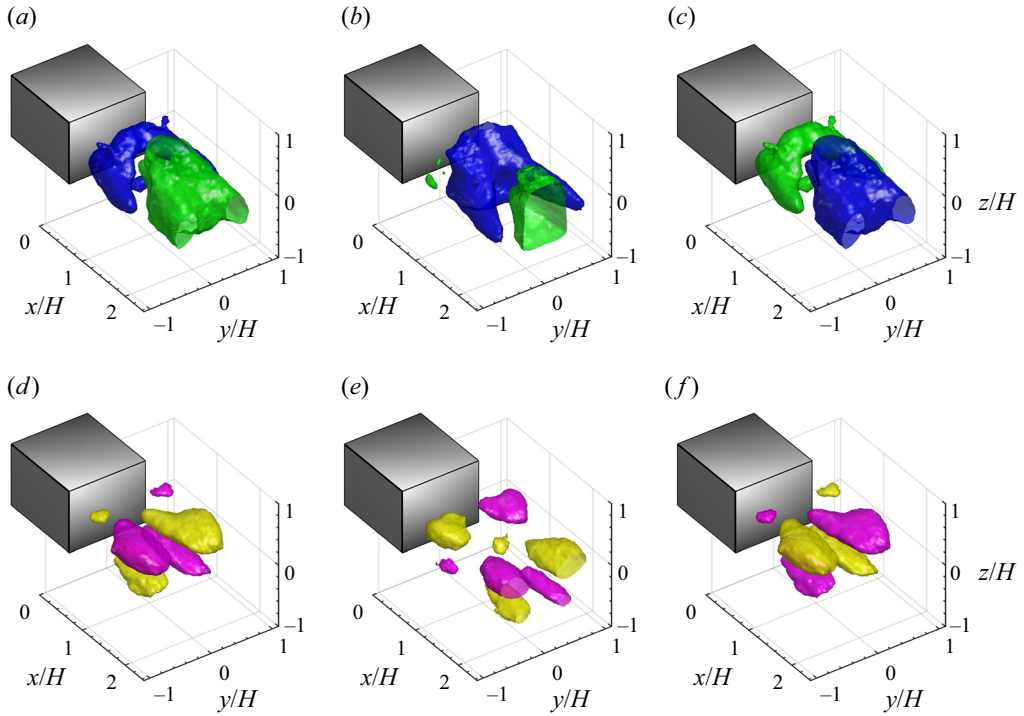
985 A19-31

Figure 21. Visualizations of the w_{ROM} and v_{ROM} of the SPOD mode at $St_H = 0.164$ at (a,d) $\Phi_1 = 0.8\pi$, (b,e) $\Phi_2 = 1.3\pi$ and (c,f) $\Phi_3 = 1.8\pi$. In $(a–c)$, the green isosurface shows $w_{ROM} = +0.1$, and blue shows $w_{ROM} = -0.1$. In $(d–f)$, yellow isosurface shows $v_{ROM} = +0.1$, and pink shows $v_{ROM} = -0.1$.
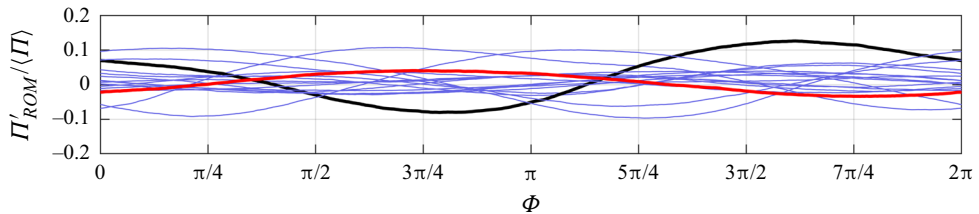

Figure 22. The normalized fluctuations of separation volume $\Pi'/\langle\Pi\rangle$ obtained from U_{ROM} of the SPOD modes within $0.123 \leq St_H < 0.218$ range. The black and red lines indicate $St_H = 0.164$ and 0.218, respectively. The blue lines show other St_H values in zone C.

bubble experiences simultaneous streamwise stretching and upward motion, followed by simultaneous streamwise contraction and downward motion. The Π' variations for the mode at $St_H = 0.218$ are smaller than the variations for $St_H = 0.164$, which is consistent with its weaker structures observed in figure 18. The magnitude of volume fluctuations is comparable to those of the swinging motion seen in figure 17 but smaller than the bi-stable motion illustrated in figure 12.

The present investigation highlights that the shedding of a pair of counter-rotating quasi-streamwise vortices is the primary mechanism behind vortex shedding, leading to regions of spanwise and vertical velocity fluctuations. Notably, flow visualization experiments conducted by Grandemange *et al.* (2012) at $Re_H = 365$ also indicate the presence of alternating quasi-streamwise vortices shed from the centre of the toroid,
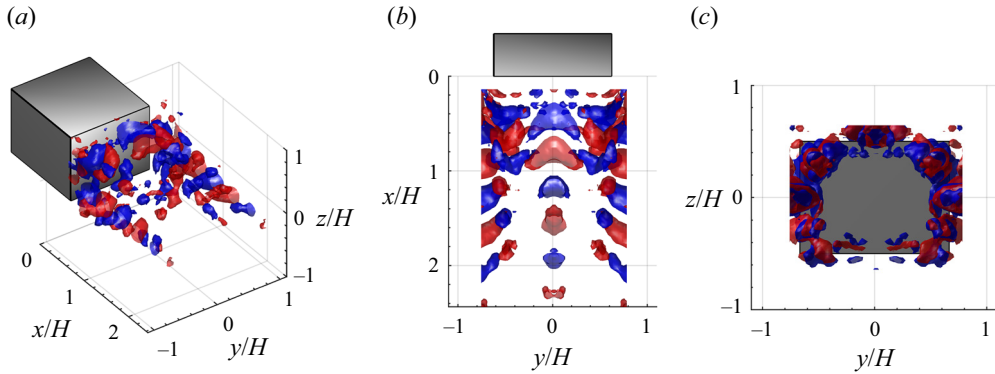
Figure 23. Spatial organization of the first SPOD mode at $St_H = 1.147$ in (*a*) isometric view, (*b*) top view and (*c*) back view. The red and blue isosurfaces show $\Psi_{u,l}/U_\infty = \pm 0.03$ for $l = 169$.

although they referred to them as vortex loops. Similarly, phase-averaged visualizations by Evstafyeva *et al.* (2017) based on simulations at $Re_H = 435$ showed that vortex shedding primarily involved quasi-streamwise structures extending from the toroid's centre and skewed towards one spanwise side. Based on analysing the coherence function and spectra of hot-wire measurements at Re_H of 9.2×10^4, Grandemange *et al.* (2013) suggested that separate vortex loops shed from the vertical and horizontal edges of the rear face at different frequencies. They explained that the rotational direction of successive vortex loops shed from the horizontal edges alternate, while the rotation direction of successive vortices shed from the vertical edge remained consistent due to the spanwise bi-stability. Grandemange *et al.* (2013) noted the difficulty of presenting a combined sketch of the two shedding loops due to their distinct frequencies. The simulation conducted by Lucas *et al.* (2017) also provides some evidence of one-sided vortex loops shed in instantaneous visualizations. However, at the high Re_H of 4.0×10^5, the cluttered nature of the vortical structures made it challenging to accurately characterize the vortex topology. These vortex loops bear resemblance to the shedding of instantaneous hairpin-like structures observed just before the wake switching in numerical simulations by Dalla Longa *et al.* (2019) and Fan *et al.* (2020).

6.4. *Shear layer instability*

To examine the spatio-temporal dynamics of fluctuations within the $1.024 \leq St_H < 1.228$ range, the SPOD mode at $St_H = 1.147$ is presented in figure 23. This St_H corresponds to the peak in the eigenvalue spectrum shown in figure 7. Figure 23 shows small structures with alternating signs along the shear layers. Stronger structures are observed in the top and vertical shear layers while the structures in the lower shear layer are weak and barely visible in figure 23. Supplementary movie 11 demonstrates that these structures evolve along the shear layers and gradually diminish as they move downstream.

To understand the source of the structures observed in figure 23, their Strouhal number is calculated using the local thickness of the shear layer (ξ), which is obtained based on the thickness of the layer with intense vorticity measured using planar PIV. At $x/H = 0.3$, ξ is found to be $0.16H$ for both upper and lower shear layers. The Strouhal number of the structures, calculated as $St_\xi = f \times \xi/U_\infty$ with $f = 15.14$ Hz and $\xi = 0.16H$, is determined to be 0.18. This value is similar to the Strouhal number of 0.2 obtained from the linear stability theory for Kelvin–Helmholtz instabilities (Monkewitz & Huerre 1982).
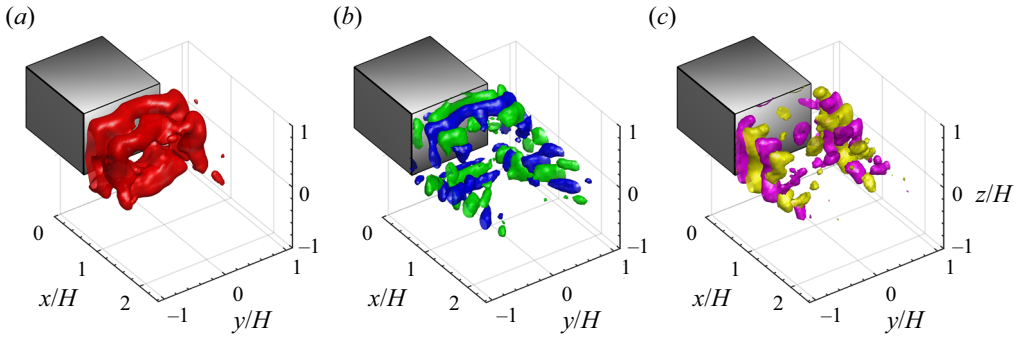
Figure 24. Visualizations of ROM obtained for the SPOD mode at $St_H = 1.147$ at $\Phi = 0$. (*a*) The red isosurface shows $Q^* = 0.32$, (*b*) green and blue isosurface shows $w_{ROM} = +0.035$ and -0.035, respectively, (*c*) yellow and pink isosurfaces show $v_{ROM} = +0.035$ and -0.035, respectively.

Therefore, the analysis suggests that the structures observed in figure 23 are generated by the instabilities of the shear layers. The structures observed in figure 23 are consistent with those identified in the SPOD mode at $St_H \approx 1$ by Haffner *et al.* (2020). They applied SPOD analysis to velocity fields in the streamwise–spanwise plane and light intensity images in the wall-normal–streamwise plane. Their analysis revealed that the spatial pattern of the SPOD mode at $St_H \approx 1$ is linked to the interaction between the recirculating flow and the shear layer on the opposite side, leading to the amplification of shear layer instabilities and the roll-up of vortices.

Figure 24(*a*) displays the isosurface of Q^* for $St_H = 1.147$, computed using the velocity fields obtained from the ROM at $\Phi = 0$. The visualization shows two successive toroidal vortical structures that resemble the toroidal vortex of the mean flow. Supplementary movie 12 corresponds to the animation of figure 24, which shows that these toroidal vortices gradually weaken and eventually vanish as they move downstream. In addition, figure 24(*b*) presents the vertical velocity fluctuations, which consist of small structures along the span of the top and side shear layers. In contrast, the spanwise velocity fluctuations in figure 24(*c*) are predominantly observed in the side shear layers. After examining the spatial variations of the barycentre and the fluctuations of separation volume, it was found that they are negligible compared with those of previously discussed flow motions. As a result, the corresponding plots are not included here to keep the discussion short.

7. Conclusion

The objective of this study was to address the knowledge gaps regarding the dynamics of turbulent motions in the wake of an Ahmed body. These gaps are primarily attributed to limitations in measurements and the shortcomings of the commonly used space-only POD technique to effectively differentiate flow motions at different frequencies. To overcome these limitations, the combination of time-resolved 3-D flow measurements using tomo-PIV and SPOD of the flow fields was employed. This approach allowed for the identification and characterization of coherent motions within the wake flow at discrete frequencies. The investigations were carried out in a water channel at a Reynolds number of $Re_H = 10\,000$ and with an elevated ground clearance of $0.37H$ between the Ahmed body and the underlying flat plate. Here, H is the height of the Ahmed body.

The frequency spectrum of the first and second modes in SPOD analysis revealed the presence of four distinct types of flow motions. Each motion corresponds to a specific range of the Strouhal number (St_H) and exhibits a unique flow dynamics. The findings of this study shed light on the phenomena of bi-stability, swinging/flapping motions, vortex shedding and shear layer instability for Ahmed body's wake. Here is a brief description of each motion:

(i) Bi-stability motion: at the lower end of the frequency spectrum where $St_H < 0.014$, the wake exhibited a bi-stable motion that accounts for 17.5 % of the energy in the first SPOD mode. This motion tilted the separation bubble in the spanwise direction and as a result the barycentre of the separation bubble moved between two spanwise locations. During the asymmetric states, the wake consisted of a toroidal vortex that was tilted and attached to a strong streamwise vortex. The streamwise vortex was located along the spanwise centre of the wake and closer to the upper edge of the Ahmed body. It generated a strong spanwise motion towards the separation bubble and the wake barycentre. When the wake transitioned from an asymmetric to a symmetric state, the toroidal vortex became symmetric, and the streamwise vortex vanished. In the opposing asymmetric state, the streamwise vortex reappeared at the same location wake, and its rotational direction reversed. The ROM demonstrated that the volume of the separation bubble increased by up to 45 % when the separation bubble was tilted in the spanwise direction into its asymmetric state.

(ii) Swinging/flapping motion: the swinging (or flapping) motion was observed within the range of $0.014 \leq St_H < 0.123$ and accounted for 14.2 % and 18.6 % of the energy of the first and second SPOD modes, respectively. The motion at each St_H resulted in small spanwise or vertical movements of the wake barycentre through symmetry-breaking or symmetry-preserving SPOD modes, respectively. The spanwise movements of the barycentre occurred in isolation without any streamwise or vertical displacements. These spanwise movements differ from those of the bi-stability motion, as they were several times smaller than the spanwise motion associated with bi-stability. Furthermore, in the asymmetric state of the spanwise swings, the wake consisted of a skewed toroidal vortex without the streamwise vortex seen in the asymmetric state of the bi-stability motion. The results demonstrated that the vertical swings occurred along with streamwise movement of the barycentre and expansion/contraction of the separation volume, characteristics associated with the bubble-pumping motion. However, it is important to note that the variations in the separation volume were small, reaching a maximum of 10 % of the mean volume of the separation bubble. Also, in-phase fluctuations of the vertical swinging motions were only observed at the two spanwise sides of the rear face.

(iii) Vortex shedding: the vortex-shedding motions were observed in the range of $0.123 \leq St_H < 0.234$ and accounted for 31.4 % and 27.3 % of the energy in the first and second SPOD modes, respectively. The vortex-shedding phenomenon primarily involved the shedding of a pair of counter-rotating quasi-streamwise vortices from the centre of the toroid. They also induced vertical and spanwise velocity fluctuations that advected downstream with them. The shedding of these quasi-streamwise vortices resulted in the wake's barycentre following an oblique path in the streamwise-vertical plane. Compared with the bi-stability and swirling motions, the vertical displacement associated with vortex shedding was larger. Notably, the analysis revealed that the magnitude of variation in the separation bubble volume caused by vortex shedding was comparable to that induced by vertical swinging motions.

(iv) Shear layer instabilities: these motions correspond to the Kelvin–Helmholtz instability within the shear layers and were observed in the range of $1.024 \leq St_H < 1.228$. Despite their presence, these motions contribute to a mere 2 %–3 % of the energy in the first and second SPOD modes and have negligible effects on the wake barycentre and the volume of the separation bubble. The topology associated with the shear layer instabilities primarily consists of weak toroidal vortices that rapidly dissipate as they advect downstream. The vortices induce small-scale vertical velocity fluctuations within the top shear layer and spanwise velocity fluctuations within the side shear layers. However, their influence on the overall wake dynamics, as indicated by the minimal modifications to the wake barycentre and separation bubble volume, is relatively insignificant.

It is important to note that the above observations have been made at $Re_H = 10\,000$ and the Ahmed body model was installed with a large ground clearance. Further evaluations of turbulent structures at higher Re_H and with a ground clearance more representative of road vehicles should be conducted in the future when experimental or numerical capabilities permit.

Supplemental movies. Supplementary movies are available at https://doi.org/10.1017/jfm.2024.288.

Declaration of interests. The authors report no conflict of interest.

Author ORCIDs.
S. Ghaemi https://orcid.org/0000-0001-8893-2993.

REFERENCES

AHMED, S.R., RAMM, G. & FALTIN, G. 1984 Some salient features of the time-averaged ground vehicle wake. *SAE Tech. Paper* 840300.

ATKINSON, C. & SORIA, J. 2009 An efficient simultaneous reconstruction technique for tomographic particle image velocimetry. *Exp. Fluids* **47** (4–5), 553.

BERGER, E., SCHOLZ, D. & SCHUMM, M. 1990 Coherent vortex structures in the wake of a sphere and a circular disk at rest and under forced vibrations. *J. Fluids Struct.* **4**, 231–257.

BEWLEY, G.P., SREENIVASAN, K.R. & LATHROP, D.P. 2008 Particles for tracing turbulent liquid helium. *Exp. Fluids* **44**, 887–896.

BOOYSEN, A., DAS, P. & GHAEMI, S. 2022 Large-scale 3D-PTV measurement of Ahmed-body wake in crossflow. *Exp. Therm. Fluid Sci.* **132**, 110562.

BRASLOW, A.L. & KNOX, E.C. 1958 Simplified method for determination of critical height of distributed roughness particles for boundary-layer transition at Mach numbers from 0 to 5. *NACA TN* 4363.

CABITZA, S. 2013 Active control of the wake from a rectangular-sectioned body. PhD thesis, Imperial College London.

CADOT, O., EVRARD, A. & PASTUR, L. 2015 Imperfect supercritical bifurcation in a three-dimensional turbulent wake. *Phys. Rev.* E **91** (6), 063005.

CROLL, R.H., GUTIERREZ, W.T., HASSAN, B., SUAZO, J.E. & RIGGINS, A.J. 1996 Experimental investigation of the ground transportation systems (GTS) project for heavy vehicle drag reduction. *Tech. Rep.*, *SAE Tech. Paper*.

DALLA LONGA, L., EVSTAFYEVA, O. & MORGANS, A.S. 2019 Simulations of the bi-modal wake past three-dimensional blunt bluff bodies. *J. Fluid Mech.* **866**, 791–809.

DAS, P. & GHAEMI, S. 2021 Light-scattering of tracer particles for liquid flow measurements. *Meas. Sci. Technol.* **32**, 065302.

DUELL, E.G. & GEORGE, A.R. 1999 Experimental study of a ground vehicle body unsteady near wake. *SAE Trans.* **108** (6; Part 1), 1589–1602.

ELSINGA, G.E. & WESTERWEEL, J. 2012 Tomographic-PIV measurement of the flow around a zigzag boundary layer trip. *Exp. Fluids* **52**, 865–876.

EVRARD, A., CADOT, O., HERBERT, V., RICOT, D., VIGNERON, R. & DÉLÉRY, J. 2016 Fluid force and symmetry breaking modes of a 3D bluff body with a base cavity. *J. Fluids Struct.* **61**, 99–114.

EVSTAFYEVA, O., MORGANS, A.S. & DALLA LONGA, L. 2017 Simulation and feedback control of the Ahmed body flow exhibiting symmetry breaking behaviour. *J. Fluid Mech.* **817**, R2.

FAN, Y., CHAO, X., CHU, S., YANG, Z. & CADOT, O. 2020 Experimental and numerical analysis of the bi-stable turbulent wake of a rectangular flat-backed bluff body. *Phys. Fluids* **32**, 105111.

GRANDEMANGE, M., GOHLKE, M. & CADOT, O. 2012 Reflectional symmetry breaking of the separated flow over three-dimensional bluff bodies. *Phys. Rev.* E **86**, 035302(R).

GRANDEMANGE, M., GOHLKE, M. & CADOT, O. 2013 Turbulent wake past a three-dimensional blunt body. Part 1. Global modes and bi-stability. *J. Fluid Mech.* **722**, 51–84.

GRANDEMANGE, M., GOHLKE, M. & CADOT, O. 2014 Turbulent wake past a three-dimensional blunt body. Part 2. Experimental sensitivity analysis. *J. Fluid Mech.* **752**, 439–461.

HAFFNER, Y., BORÉE, J., SPOHN, A. & CASTELAIN, T. 2020 Mechanics of bluff body drag reduction during transient near-wake reversals. *J. Fluid Mech.* **894**, A14.

HANSON, R.E., BUCKLEY, H.P. & LAVOIE, P. 2012 Aerodynamic optimization of the flat-plate leading edge for experimental studies of laminar and transitional boundary layers. *Exp. Fluids* **53**, 863–871.

HOWELL, J., SHEPPARD, A. & BLAKEMORE, A. 2003 Aerodynamic drag reduction for a simple bluff body using base bleed. *SAE Tech. Paper* 2003-01-0995.

HUNT, J.C.R., WRAY, A.A. & MOIN, P. 1988 Eddies, stream, and convergence zones in turbulent flows. In *Proceedings of the 2nd Summer Program, Centre for Turbulence Research*, pp. 193–208. Stanford University.

KANG, N., ESSEL, E.E., ROUSSINOVA, V. & BALACHANDAR, R. 2021 Effects of approach flow conditions on the unsteady three-dimensional wake structure of a square-back Ahmed body. *Phys. Rev. Fluids* **6**, 034613.

KHALIGHI, B., CHEN, K. & IACCARINO, G. 2012 Unsteady aerodynamic flow investigation around a simplified square-back road vehicle with drag reduction devices. *ASME J. Fluids Engng* **134** (6), 061101.

KHALIGHI, B., ZHANG, S., KOROMILAS, C., BALKANYI, S.R., BERNAL, L.P., IACCARINO, G. & MOIN, P. 2001 Experimental and computational study of unsteady wake flow behind a bluff body with a drag reduction device. *SAE Paper* 2001-01-1042.

LI, R., BARROS, D., BORÉE, J., CADOT, O., NOACK, B.R. & CORDIER, L. 2016 Feedback control of bimodal wake dynamics. *Exp. Fluids* **57** (10), 158.

LUCAS, J.M., CADOT, O., HERBERT, V., PARPAIS, S. & DÉLÉRY, J. 2017 A numerical investigation of the asymmetric wake mode of a squareback Ahmed body - effect of a base cavity. *J. Fluid Mech.* **831**, 675–697.

LUMLEY, J.L. 1970 *Stochastic Tools in Turbulence*. Academic Press.

MONKEWITZ, P.A. & HUERRE, P. 1982 Influence of the velocity ratio on the spatial instability of mixing layers. *Phys. Fluids* **25** (7), 1137–1143.

NEKKANTI, A. & SCHMIDT, O. 2021 Frequency-time analysis, low-rank reconstruction and denoising of turbulent flows using SPOD. *J. Fluid Mech.* **926**, A26.

PAVIA, G. 2019 *Characterisation of the Unsteady Wake of a Square-Back Road Vehicle (Version 1)*. Loughborough University.

PAVIA, G., PASSMORE, M. & SARDU, C. 2018 Evolution of the bi-stable wake of a square-back automotive shape. *Exp. Fluids* **59** (1), 20.

PAVIA, G., PASSMORE, M.A., VARNEY, M. & HODGSON, G. 2020 Salient three-dimensional features of the turbulent wake of a simplified square-back vehicle. *J. Fluid Mech.* **888**, A33.

PERRY, A.K., ALMOND, M.T., PASSMORE, M. & LITTLEWOOD, R.A. 2016*a* The study of a bi-stable wake region of a generic squareback vehicle using tomographic PIV. *SAE Intl J. Passeng. Cars – Electron. Electr. Syst.* **9**, 743–753.

PERRY, A.K., PAVIA, G. & PASSMORE, M. 2016*b* Influence of short rear end tapers on the wake of a simplified square-back vehicle: wake topology and rear drag. *Exp. Fluids* **57**, 169.

PICARD, C. & DELVILLE, J. 2000 Pressure velocity coupling in a subsonic round jet. *Intl J. Heat Fluid Flow* **21** (3), 359–364.

PLUMEJEAU, B., DELPRAT, S., KEIRSBULCK, L., LIPPERT, M. & ABASSI, W. 2019 Ultra-local model-based control of the square-back Ahmed body wake flow. *Phys. Fluids* **31**, 085103.

PODVIN, B., PELLERIN, S., FRAIGNEAU, Y., BONNAVION, G. & CADOT, O. 2021 Low-order modelling of the wake dynamics of an Ahmed body. *J. Fluid Mech.* **927**, R6.

PODVIN, B., PELLERIN, S., FRAIGNEAU, Y., EVRARD, A. & CADOT, O. 2020 Proper orthogonal decomposition analysis and modelling of the wake deviation behind a squareback Ahmed body. *Phys. Rev. Fluids* **5**, 064612.

SAMIMY, M. & LELE, S.K. 1991 Motion of particles with inertia in a compressible free shear layer. *Phys. Fluids* **A3** (8), 1915–1923.

SCARANO, F. 2012 Tomographic PIV: principles and practice. *Meas. Sci. Technol.* **24** (1), 012001.

SCHLICHTING, H. & GERSTEN, K. 2016 *Boundary-Layer Theory*, 9th edn. Springer.

SCHMID, P.J. 2010 Dynamic mode decomposition of numerical and experimental data. *J. Fluid Mech.* **656**, 5–28.

SIROVICH, L. 1987 Turbulence and the dynamics of coherent structures. I. Coherent structures. *Q. Appl. Maths* **45** (3), 561–571.

TOWNE, A., SCHMIDT, O.T. & COLONIUS, T. 2018 Spectral proper orthogonal decomposition and its relationship to dynamic mode decomposition and resolvent analysis. *J. Fluid Mech.* **847**, 821–867.

VENNING, J., MCQUEEN, T., JACONO, D.L., BURTON, D., THOMPSON, M. & SHERIDAN, J. 2022 Aspect ratio and the dynamic wake of the Ahmed body. *Exp. Therm. Fluid Sci.* **130**, 110457.

VOLPE, R., DEVINANT, P. & KOURTA, A. 2015 Experimental characterization of the unsteady natural wake of the full-scale square back Ahmed body: flow bi-stability and spectral analysis. *Exp. Fluids* **56** (5), 1–22.

WESTERWEEL, J. & SCARANO, F. 2005 A universal detection criterion for the median test. *Exp. Fluids* **39**, 1096–1100.

WIENEKE, B. 2008 Volume self-calibration for 3D particle image velocimetry. *Exp. Fluids* **45**, 549–556.